Quarterly Report for

# January 1998 - March 1998

# Stanford Geothermal Program

DE-FG07-95ID13370

# Table of Contents

# 1. MEASUREMENTS OF STEAM-WATER RELATIVE PERMEABILITY

This research project is conducted by Dr. Cengiz Satik. The aim of this project is to measure experimentally relative permeability relations for steam and water flowing simultaneously in a porous medium.

## 1.1 SUMMARY

In the last quarterly report, we reported a set of steam-water relative permeability relations obtained from a successful steady-state experiment conducted under non-adiabatic conditions. These relations showed that the relative permeabilities for both steam and water phases in porous media vary with saturation in a curvilinear fashion. The saturations in this experiment were measured by using a high resolution X-ray computer tomography (CT) scanner. In addition the pressure gradients were obtained from accurate measurements of liquid-phase pressure over regions with flat saturation profiles. These two aspects constituted a major improvement in the experimental method compared to those used in the past.

During the last quarter, another attempt was given to repeat the previous experiment with further improvements in steam and hot water injection and water supply feeding systems. Two successful relative permeability experiments were conducted for both steam-water and nitrogen-water fluid pairs with the same core holder. The core holder used in this experiment was different than the one which was used in the previous experiment. Results of the recent experiments are discussed here.

## 1.2 INTRODUCTION

The relative permeability concept is used widely to describe multiphase fluid transport through porous systems. Fluid flow in geothermal reservoirs and petroleum reservoirs are a few examples among the many other natural and artificial systems. In short, relative permeability is a dimensionless measure of permeability to individual phases during multi-phase flow in a porous medium. Typically, relative permeability to each phase is described in a functional form, traditionally as a function of one of the fluid saturations. Due to the importance of these functions, many experimental and theoretical attempts have been reported in both geothermal and oil literature. Although the applications of the subject are very wide, here we focus only on the steam-water relative permeability in the scope of geothermal reservoir engineering. Good literature reviews on the subject can be found in Satik et al. (1995) and Ambusso et al. (1996). These reviews indicate a wide range of discrepancy in the previous experimental results. The main reason for this has been identified as the difficulty in measuring saturations accurately and using incorrect pressure gradients to compute relative permeability (Ambusso et al., 1996). We overcame these difficulties by using an X-ray CT (computer tomography) scanner to measure saturation accurately and by evaluating pressure gradients within the constant saturation regions only. Recently we reported our first successful steam-water flow experiments where significant improvements were achieved in measuring saturations and collecting experimental data (Ambusso et al., 1996). The results obtained from the first experiment

suggested a linear relationship for steam-water relative permeability. In attempting to repeat these first results, significant improvements to the experimental apparatus were achieved. Finally, another successful experiment was conducted recently and steam-water relative permeability was calculated. However, these results suggested a curvilinear relationship that is different than our first results, a linear relationship (Satik, 1998). Very recently, another successful relative permeability experiment was conducted and steam-water and nitrogen-water relative permeabilities were calculated for both drainage (increasing steam saturation) and imbibition (decreasing steam saturation) processes. Unfortunately, results of this experiment revealed only three points. Agreement between these three points and the previous experimental result does not seem to be reasonable. Finally, expected results were obtained from nitrogen-water relative permeability experiment. We will discuss the details of these two experiments here.

## 1.3 EXPERIMENTAL APPARATUS AND METHOD

The details of experimental apparatus used in this experiment were described in Satik (1998). In summary, the apparatus consisted of an injection unit, and a core holder assembly. The injection unit consisted of two immersion heaters to generate steam and hot water and two liquid pumps. Two voltage controllers were used to control the temperatures of the heaters. The core holder was constructed from a peek (high temperature plastic) tube, a high temperature epoxy and several high temperature peek fittings. Temperatures along the core were measured by T-type thermocouples inserted at locations where pressure ports are located. There were eight pressure and temperature measurements along the core holder, two at the inlet and one at the outlet. Heat losses on the core body were measured by using nine heat flux sensors placed at various locations. All of the measurements during the experiment were taken by using a data acquisition system. Direct monitoring of pressures and temperatures during the experiment enabled us to determine when steady state conditions had been reached. The Berea sandstone rock sample used for these experiments had the following properties; permeability 1300 md, porosity 22%, length 43.2cm and diameter 5.00 cm. A picture of the experimental apparatus within the X-ray CT scanner is shown in Figure 1.1.

The experimental procedure was as follows. First, air inside the pore space was removed by using a vacuum pump, then the core was scanned at predetermined locations to obtain dry-core CT values. Next, deaerated water was injected into the core to saturate it completely. This step continued until the core was completely saturated with water, at which time the core was scanned again at the same locations to obtain wet-core CT values and pressure and temperature readings were again taken at this time. An interpretation software was used to calculate the porosity and saturation distributions from the *CT* values obtained during the experiment. Steady-state relative permeability experiments involve injection of varying fractions of steam and water into the core. Measurements done at each step result in a single data point on relative permeability vs. saturation curve. Starting from a completely water saturated core and injecting steam at increasing fractions will give rise to a drainage process while the opposite procedure gives rise to an imbibition process. Each step continued until steady-state conditions at which injection and production rates became the same for both steam and water and also pressures and

temperatures stabilized. At the onset of steady-state conditions, another X-ray scan was done along the core at the same locations to obtain CT values corresponding to the particular steam-water fraction. Next, the steam-water fraction was changed and the procedure was repeated (see Satik, 1998 for details).

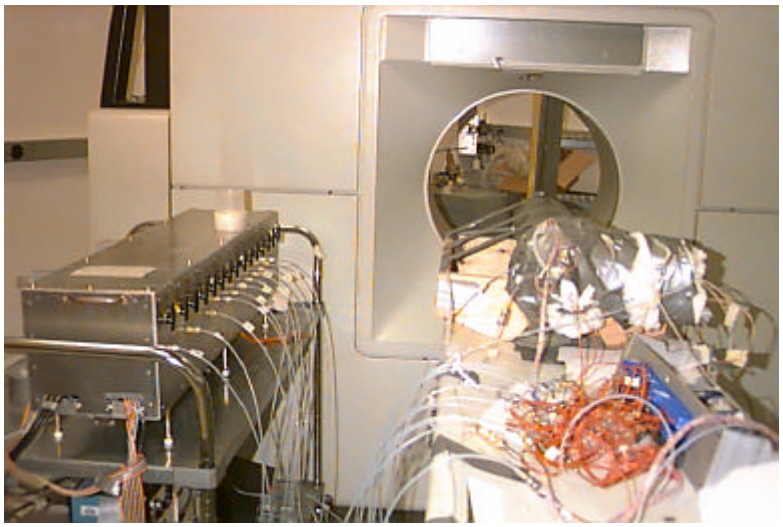

*Figure 1.1: A picture of the X-ray CT scanner and the core holder used in flow experiments.*

After mounting the core holder assembly to the CT scanner, the first step in the experiment was to determine the porosity of the core. This was achieved by taking X-ray CT scans of the core at 41 locations when it was dry and again when it was fully saturated with water. First, the core was kept under vacuum for several hours and the initial scan was performed to obtain dry-core CT values. Following this, water was injected at low flow rate (10 cc/min) for sufficiently long time (12 hours) to saturate the core completely with water. A second scan was then conducted to obtain wet-core CT values at the same locations as the dry-core CT scan. By using these two sets of images obtained it was possible to determine the porosity distribution of the core. Figure 1.2 shows porosity images obtained at four locations along the core; we obtained a total of 41 such slices during the experiment. Average porosity profiles were also calculated by averaging porosities over each slice along the core and these are shown in Figure 1.3. Average porosity of the whole core was found to be about 22%. After the porosity distribution had been determined the absolute permeability was determined by flowing water at different flow rates and measuring pressures along the core. From this test, the permeability of the core was calculated to be 1300 md.

Steady-state conditions were recognized by the stabilization of temperature and pressure. Typically stabilization took three to five hours, though some of the measurements reported here were taken after at least six hours. Once a steady state had been confirmed, the measurements of temperature and pressure were recorded together with the heat flux sensors readings. The X-ray CT scans were then taken at locations where the dry and wet scans had been taken to obtain a set of CT values. These scans were then processed into

saturation images. The average saturation profiles presented in this paper were obtained by averaging the saturation values over a cross sectional area of the core.

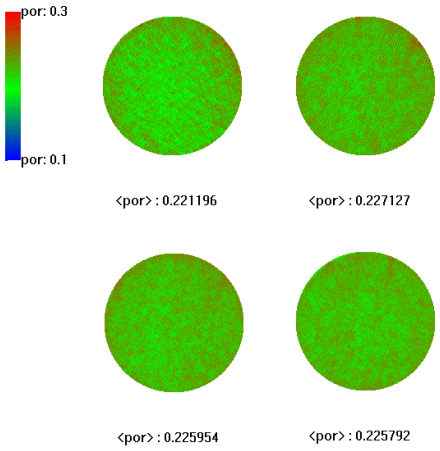


*Figure 1.2: Selected images for porosity distributions obtained from the X-ray CT scan at 1, 11, 21 and 40 cm away from the inlet of the core.*

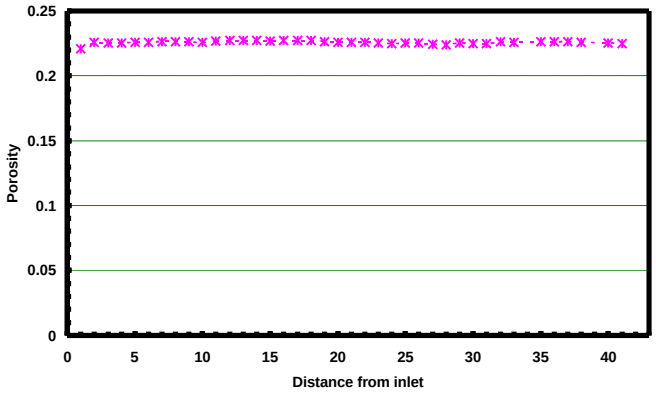


*Figure 1.3: Average porosity profiles obtained during the experiment.*

## 1.4 RESULTS AND DISCUSSION

Steam-water and nitrogen-water relative permeability functions were obtained from two experiments conducted using the same core holder. Both experiments were terminated without having any fluid leaks, proving the robustness of the new core holder design. The results obtained from these experiments are discussed below.

### 1.4.1 Steam-Water Relative Permeability Experiment

First a steam-water relative permeability experiment for both drainage and imbibition cycles was conducted under non-adiabatic conditions. During the experiment, the phase fractions of the injected fluids were changed 41 times while attempting to change the steam saturation in the core. Each of these 41 attempts, referred as steps in this

description, are summarized in Table 1.1 for drainage cycle and in Table 1.2 for imbibition cycle. All of the flow rates shown in both tables are given as water equivalent. During drainage minimum and maximum injection rates were 0.1 and 8.5 for steam while they were 1, 10 $cm^3$/min, respectively. To be consistent, the same injection rate scheme was followed during imbibition cycle. At the end of each step an X-ray CT scan was taken and saturation distributions were calculated. Steam-water relative permeabilities along the flat saturation regions were calculated using the Darcy Equation modified for this problem (see Satik, 1998).

To investigate the gravity segregation issue, each saturation distribution image was examined after calculation. In general, all of the images indicated fairly uniform saturations for the most sections of the core at all flow rates, except sections closer to the inlet end of the core possibly due to somewhat stronger inlet end-effects. In Figure 1.4 we show steam saturation distributions calculated from X-ray CT data at four locations along the core. As shown in the images, more water exists at the bottom while more steam is at the top of the cross-sectional area at 1 and 11 cm (Figure 1.4a and b) while fairly uniform saturation distributions are seen in the last two images. The examination of all of the 41 slices at all of the steps revealed that steam and hot water injected were well mixed at about three cm from the inlet, resulting in saturated fluid conditions.

Figures 1.5a and b show some of the average saturation profiles obtained during the experiment for both drainage and imbibition cycles. The average steam saturations were calculated averaging all of the saturation values on each of 41 slices. In general, all of the average saturation profiles show a slight decreasing trend from the injection end to the production end which was also observed in the numerical simulation results for the non-adiabatic case (see Satik, 1998). As seen from all of the steps given in the figure, the values of saturation are never really constant but change gradually. The saturation profiles shown in Figure 1.5a and b also reveal another interesting feature. The capillary end-effects and heat losses become very important at low steam flow rates.

*Table 1.1: Summary of the some of the steps used during the drainage cycle of the steam-water relative permeability experiment.*

| Step | $q_{water}$, cc/min | $q_{steam}$, cc/min | Time elapsed,hr |
|---|---|---|---|
| 6 | 13 | 0.1 | 88.67 |
| 7 | 10 | 0.5 | 137.5 |
| 8 | 10 | 0.7 | 140.28 |
| 9 | 10 | 0.7 | 143.28 |
| 10 | 10 | 0.7 | 145.15 |
| 11 | 8 | 0.7 | 151.67 |
| 12 | 8 | 1 | 165.4 |
| 13 | 8 | 1 | 167 |
| 14 | 8 | 1.3 | 168.97 |
| 15 | 8 | 1.3 | 171.95 |
| 16 | 6 | 2 | 185.05 |
| 17 | 4 | 3 | 187.93 |
| 18 | 4 | 3 | 190.98 |
| 19 | 2 | 4 | 197.37 |
| 20 | 2 | 5 | 208.4 |
| 21 | 1.5 | 7 | 212.07 |
| 22 | 1.5 | 7 | 213.92 |
| 23 | 1.5 | 8.5 | 215.65 |
| 24 | 1.5 | 8.5 | 216.67 |
| 25 | 1 | 8 | 234.45 |
| 26 | 1 | 8 | 237.3 |
| 27 | 2 | 8 | 238.8 |
| 28 | 2 | 8 | 240.83 |
| 29 | 2 | 8 | 243.37 |

*Table 1.2: Summary of the steps used during the imbibition cycle of the steam-water relative permeability experiment.*

| Step | $q_{water}$, cc/min | $q_{steam}$, cc/min | Time elapsed,hr |
|---|---|---|---|
| 0 | 2 | 8 | 243.37 |
| 1 | 2 | 8 | 245.7 |
| 2 | 1 | 8 | 256.63 |
| 3 | 1.5 | 7 | 262.48 |
| 4 | 2 | 5 | 269.55 |
| 5 | 2 | 4 | 279.17 |
| 6 | 4 | 3 | 287.52 |
| 7 | 6 | 2 | 302.9 |
| 8 | 8 | 1.3 | 307.91 |
| 9 | 8 | 0.7 | 312.55 |
| 10 | 10 | 0.5 | 330.22 |
| 11 | 10 | 0.5 | 333.57 |
| 12 | 10 | 0.5 | 334.83 |

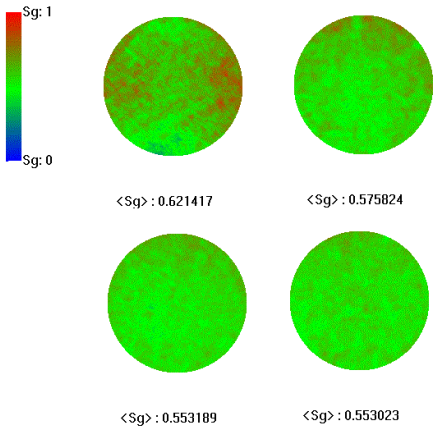


*Figure 1.4: Selected images for steam saturation distributions obtained from the X-ray CT scan at 1, 11, 21 and 40 cm away from the inlet of the core.*

Figures 1.6 and 1.7 show some of the steady-state temperature and pressure profiles for both drainage and imbibition cycles. As described in the experimental apparatus section, the thermocouples were inserted through the fittings for the pressure taps. Thus the thermocouples made direct contact with the core sample. This was done in order to obtain the temperature measurements at the core face where the pressure readings were taken. The pressures were measured by using teflon tubes attached to the core holder body. To ensure that the readings were for the water phase these tubes were filled completely with

water up to the transducers. By this method water in the tubes was assumed to be in contact with water in the core. In general all of the temperature and pressure measurements reflected the expected behavior i.e. decreasing values along the core from the injection end due to heat losses.

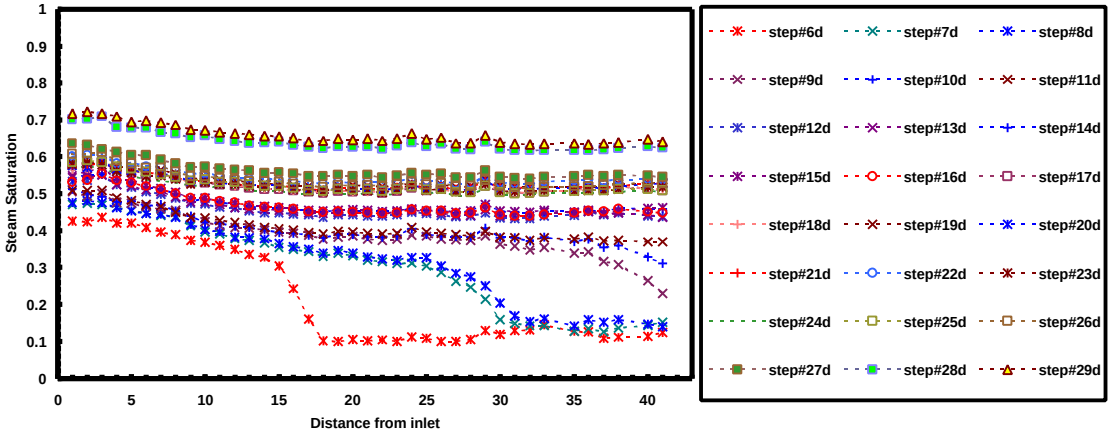


*(a)*

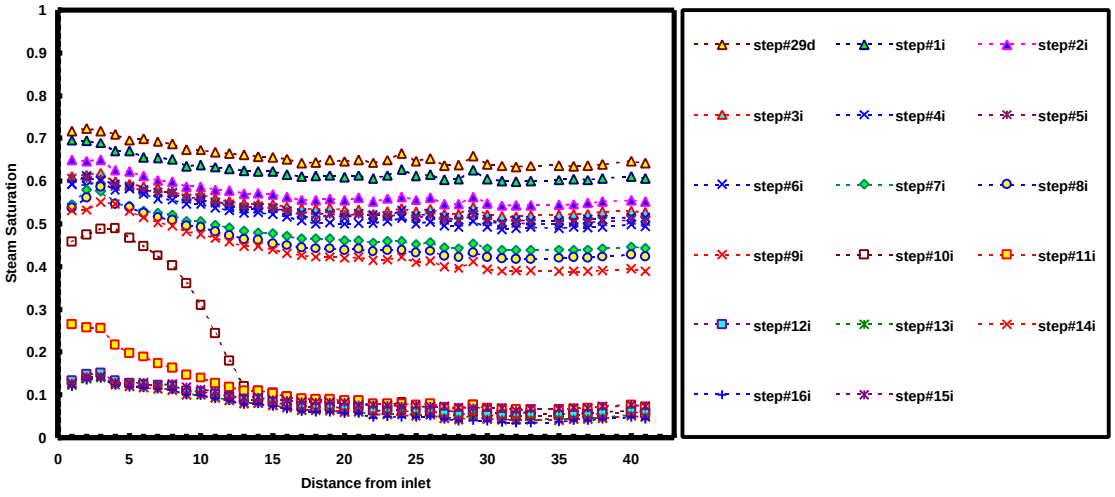


*(b)*

*Figure 1.5: Average steam saturation profiles for some of the steps conducted during the experiment for (a) drainage and (b) imbibition cycles.*

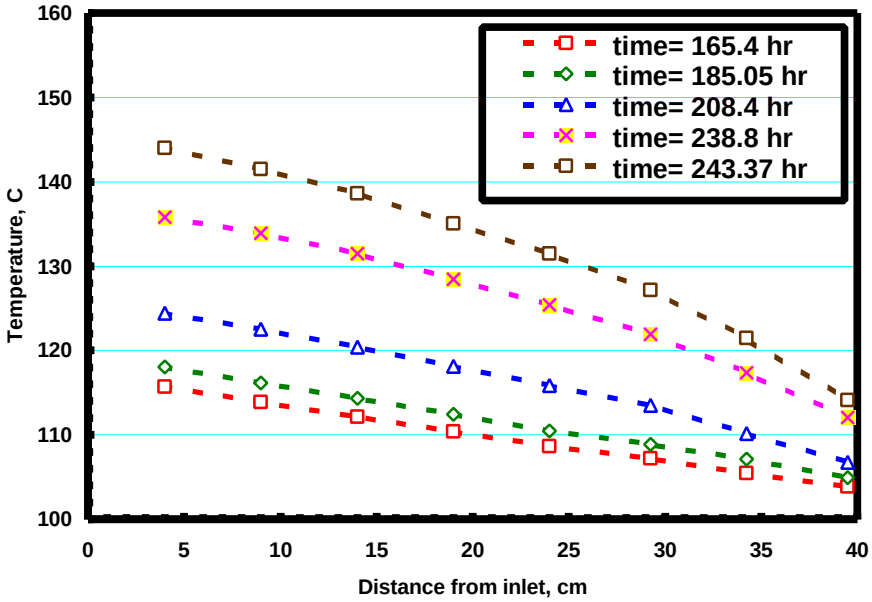


*(a)*

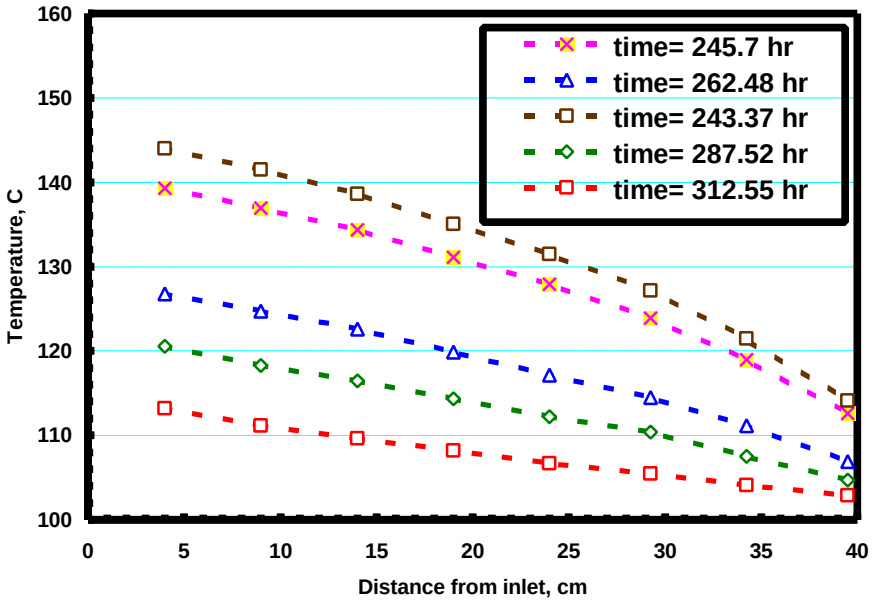


*(b)*

*Figure 1.6: Temperature profiles for some of the steps conducted during the steam-water relative permeability experiment for (a) drainage and (b) imbibition cycles.*

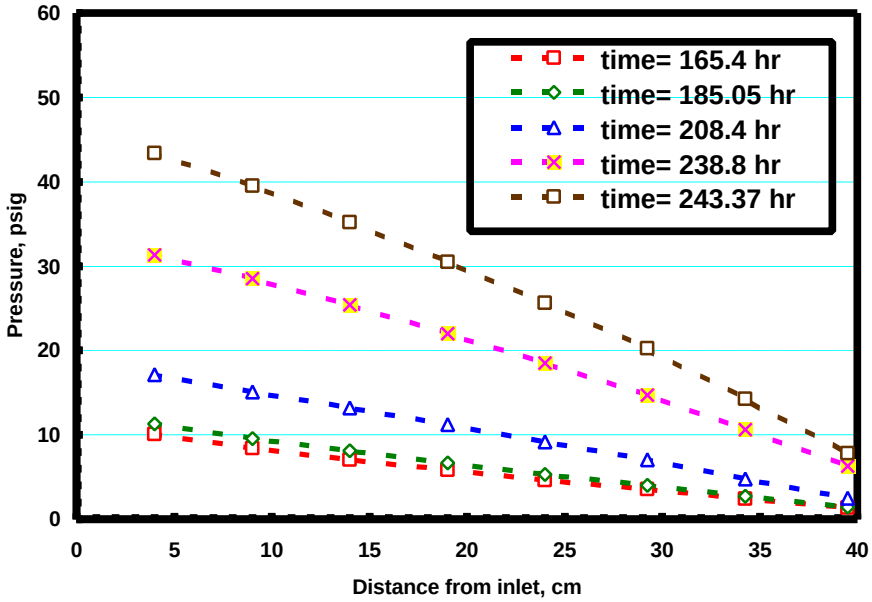


*(a)*

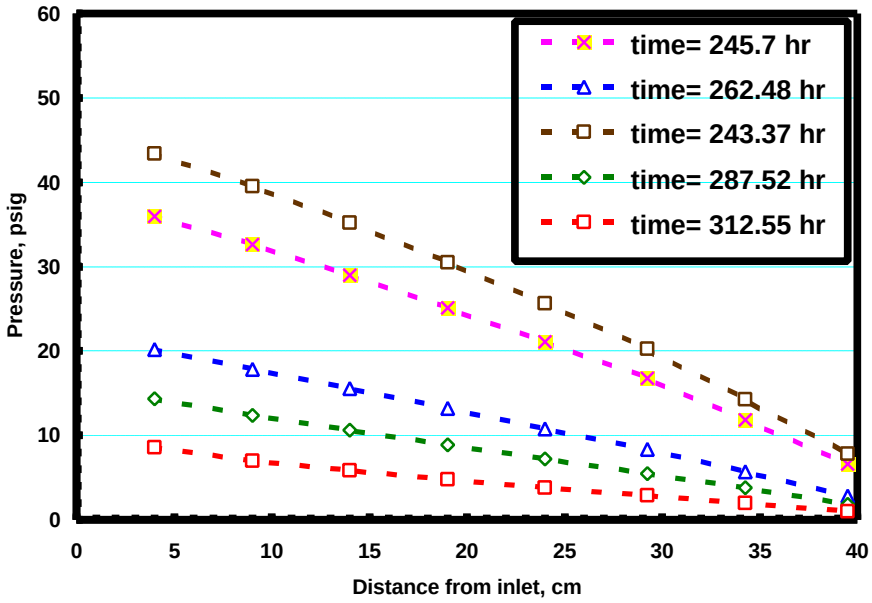


*(b)*

*Figure 1.7: Pressure profiles for some of the steps conducted during the steam-water relative permeability experiment for (a) drainage and (b) imbibition cycles.*

In order to calculate relative permeabilities, accurate knowledge of flowing mass fractions and pressures along the length of the core with a flat saturation is essential. To evaluate the flowing fractions, one needs to know the injected enthalpy and steam quality and the

heat losses along the core. Heat losses along the core body were computed directly from the measurements of the heat flux. To determine the flowing fractions at a particular point, the heat losses at the point under consideration were evaluated and subtracted from the total energy at the injection point (Satik, 1998).

Finally, in Figures 1.8a and b, we show the relative permeability curves calculated from the recent experimental data for drainage and imbibition cycles, respectively. Surprisingly, the steam and water relative permeability curves obtained from this experiment show unreasonable values. Steam relative permeability values are mostly greater than one while water relative permeabilities are always less than one. Currently we are investigating possible causes for this unusual behavior. Therefore these results do not agree with our previous results which suggested a curvilinear relationship with somewhat smaller steam relative permeabilities. In Figure 1.9, the steam-water relative permeability relations given in Figure 1.8 are compared to our previous results. Agreement is very poor. Further investigations to explain these unusual behaviors are in progress. We also plan to repeat the experiment with the same apparatus in order to confirm these recent results since the core holder is reusable.

### 1.4.2 Nitrogen-Water Relative Permeability Experiment

Upon the completion of the last step in the steam-water relative permeability experiment, the core was brought to conditions of 100% water saturation at high temperature. The nitrogen–water relative permeability experiment was then initiated by injecting nitrogen/water mixture at a known fraction. As in the previous experiment, we conducted both drainage and imbibition cycles and calculated the corresponding relative permeabilities from the results obtained.

During this experiment, the gas fractions of the injected fluids were changed 17 times while attempting to change the nitrogen saturation in the core. Each of these 17 steps are summarized in Table 1.3. All of the gas flow rates shown in the table are given at standard conditions. During the experiment, the nitrogen injection rate was changed between 2 and 200 $cm^3$/min while the water injection rate was changed between 0.5 an 18 $cm^3$/min. To be consistent, the injection rate scheme used during drainage was also followed during the imbibition cycle. Nitrogen-water relative permeabilities along the flat saturation regions were finally calculated using Darcy Equation modified for this problem.

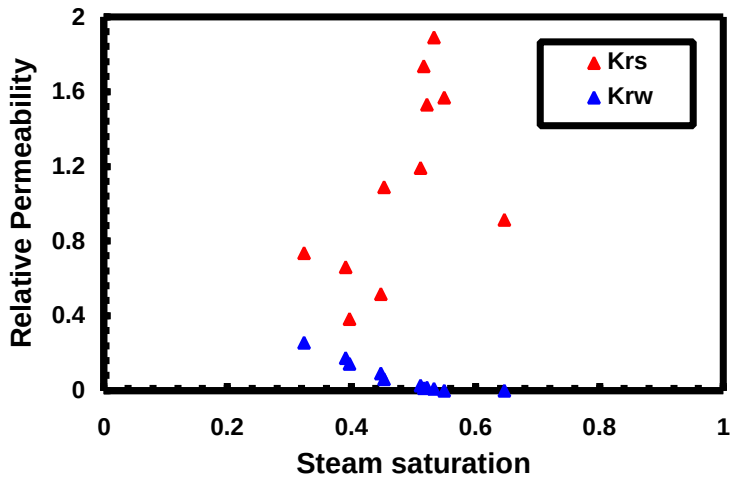


*(a)*

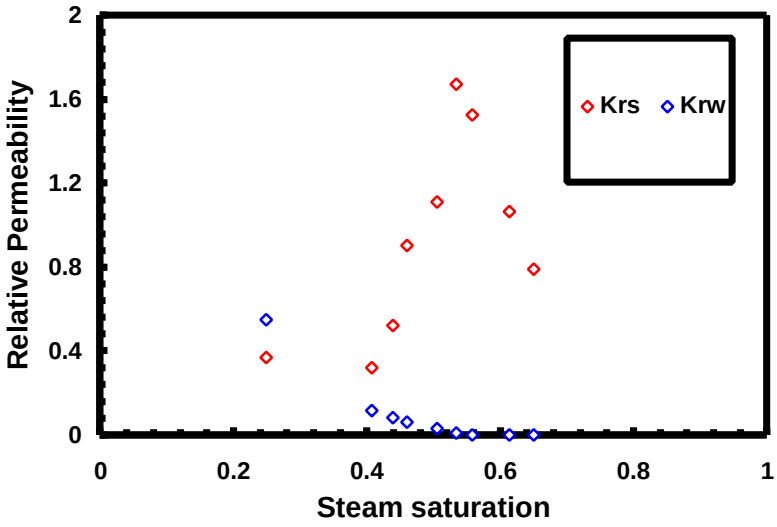


*(b)*

*Figure 1.8: Steam-water relative permeability for (a) drainage and (b) imbibition cycles.*

As in the steam-water flow experiment, an X-ray CT scan was taken at the end of each step and saturations were calculated. Again, each saturation distribution image was examined after calculation to check the gravity segregation issue. In general, we found all of the images to have uniform saturation distributions for the most sections of the core at all flow rates. Figures 1.10a and b show all of the average saturation profiles obtained during this experiment for both drainage and imbibition cycles. In general, all of the average nitrogen saturation profiles show a slight decreasing trend from the injection end to the production end. All of the steps shown in Figures 1.10a and b show that nitrogen saturations change gradually. Figures 1.11 and 1.12 show all of the steady-state temperature and pressure profiles for both drainage and imbibition cycles obtained during the nitrogen-water relative permeability experiment. In general all of the temperature and

pressure measurements reflected the expected behavior i.e. decreasing values along the core from the injection end due to fluid flow and heat losses. Finally, using the Darcy equation, relative permeabilities to nitrogen and water were calculated. The results are shown in Figure 1.13. The nitrogen-water relative permeability curves behave in a curvilinear fashion. In this case, however, the magnitudes of nitrogen-water relative permeabilities are significantly smaller than those of steam-water. This result is expected since steam and water phases are interchangeable due to the phase change mechanism.

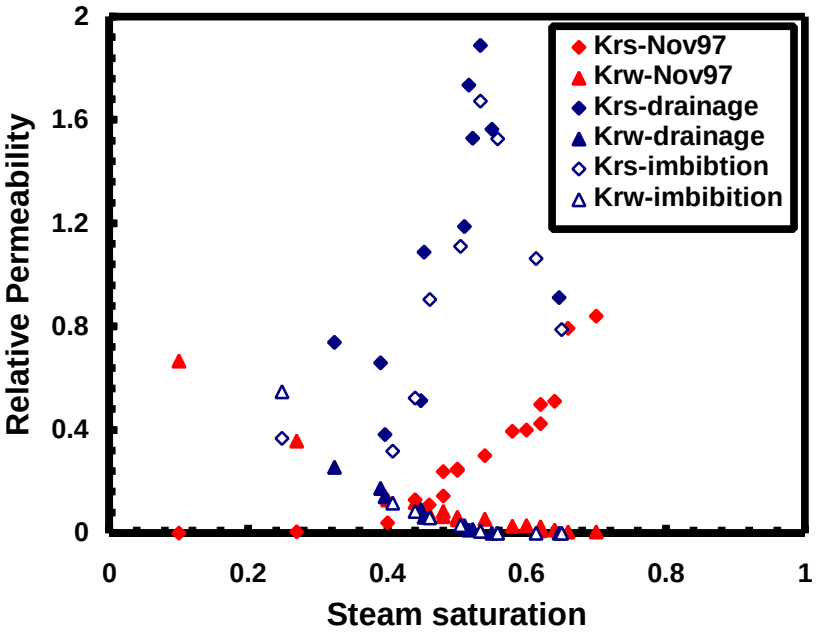


*Figure 1.9: Comparison of steam-water relative permeability curves.*

*Table 1.3: Summary of the steps used during the nitrogen-water relative permeability experiment.*

| Step | $q_{water}$, cc/min | $q_{nitrogen}$, cc/min | Time elapsed,hr |
|---|---|---|---|
| 1 | 18 | 2 | 14.33 |
| 2 | 16 | 4 | 19.15 |
| 3 | 16 | 4 | 22.32 |
| 4 | 16 | 4 | 24.17 |
| 5 | 12 | 8 | 37.5 |
| 6 | 8 | 12 | 41.58 |
| 7 | 4 | 16 | 48.067 |
| 8 | 2 | 32 | 59.25 |
| 9 | 1 | 64 | 66.77 |
| 10 | 0.5 | 128 | 72.47 |
| 11 | 0 | 200 | 84.58 |
| 12 | 1 | 64 | 108.7 |
| 13 | 2 | 32 | 115.08 |
| 14 | 4 | 16 | 122.72 |
| 15 | 12 | 8 | 136.17 |
| 16 | 16 | 4 | 144.37 |
| 17 | 18 | 2 | 155.22 |

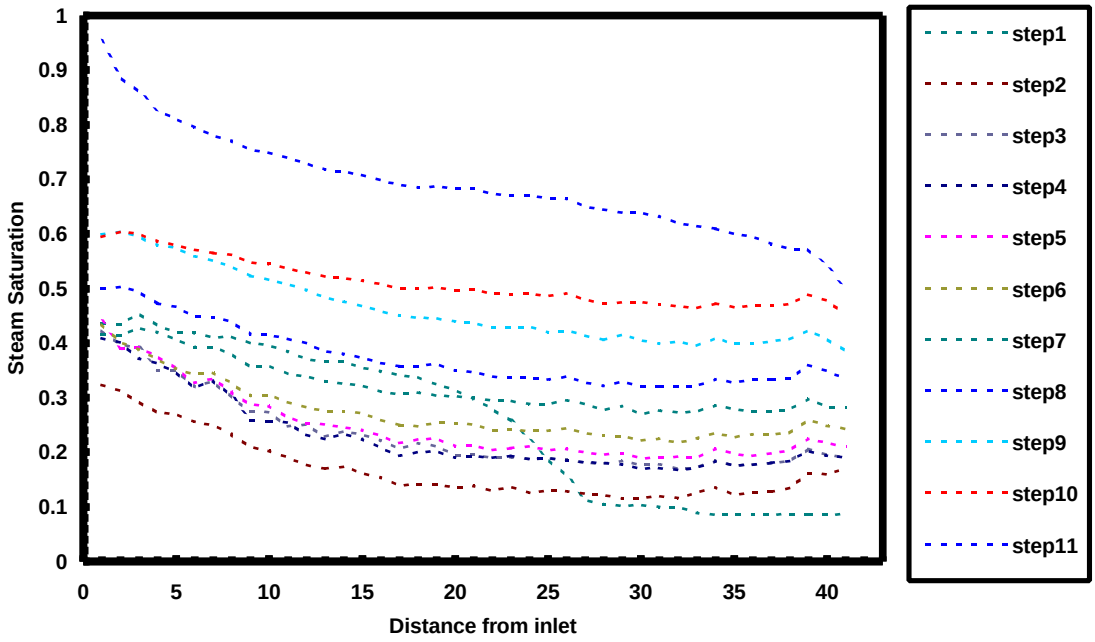


*(a)*

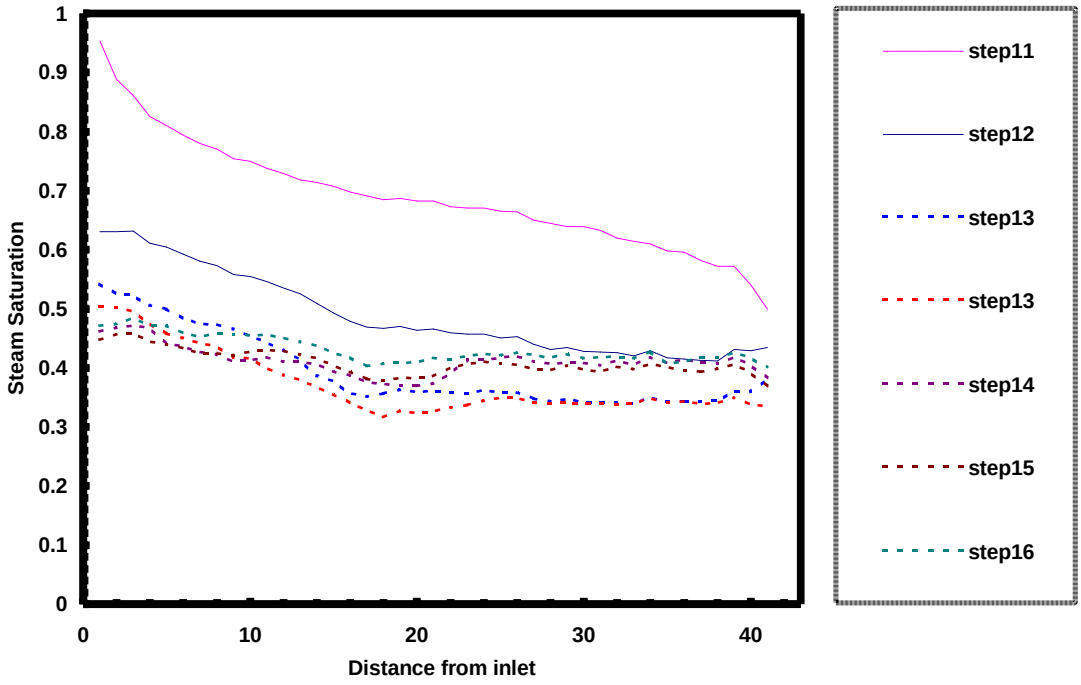


*(b)*

*Figure 1.10: Average steam saturation profiles for some of the steps conducted during the experiment for (a) drainage and (b) imbibition cycles.*

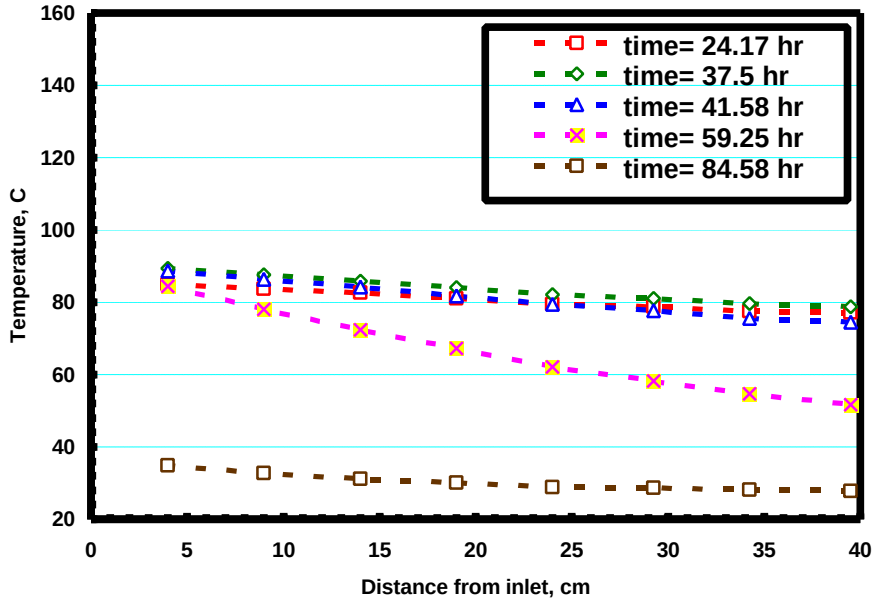


*(a)*

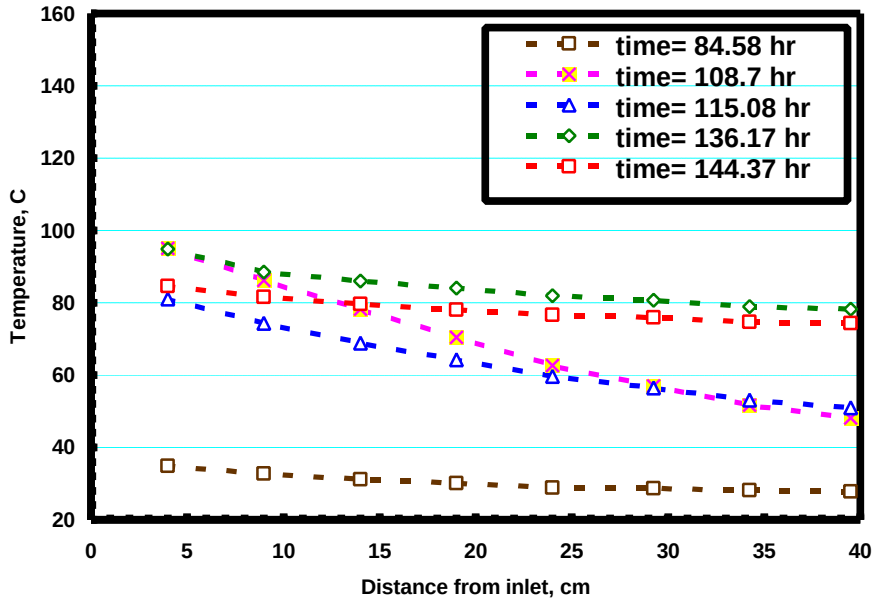


*(b)*

*Figure 1.11: Temperature profiles for some of the steps conducted during the nitrogen-water flow experiment for (a) drainage and (b) imbibition cycles.*

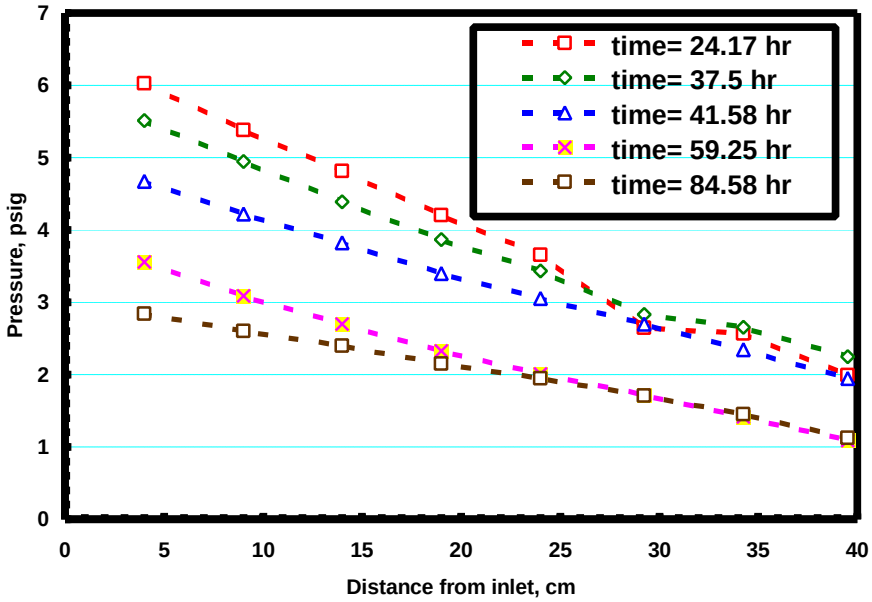


*(a)*

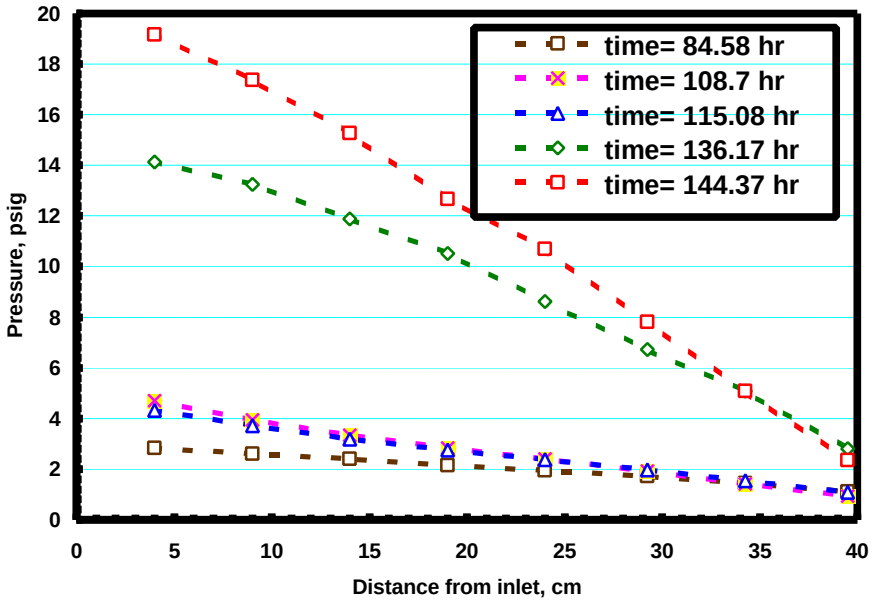


*Figure 1.12: Pressure profiles for some of the steps conducted during the nitrogen-water flow experiment for (a) drainage and (b) imbibition cycles.*

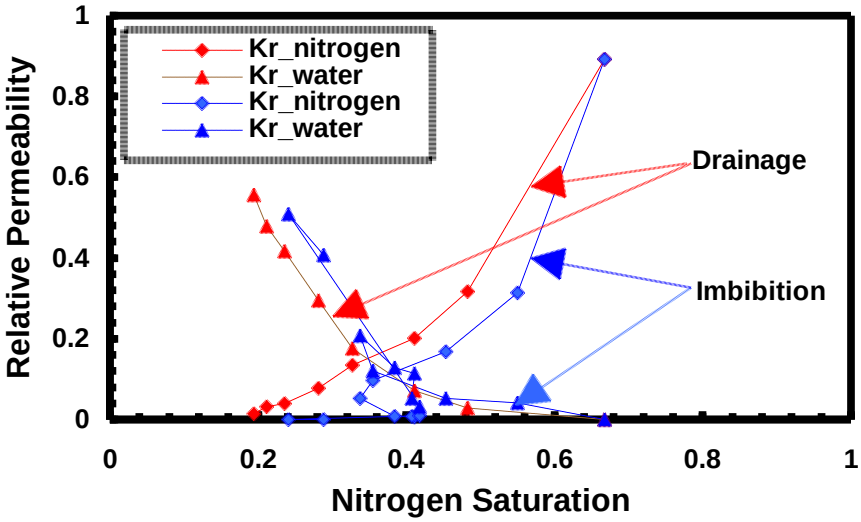


*Figure 1.13: Nitrogen-water relative permeabilities obtained from the steady-state experiment for drainage and imbibition cycles.*

# 2. MODELING MULTIPHASE BOILING FLOW IN POROUS AND FRACTURED MEDIA

This research project is currently being conducted by Research Assistant Glenn Mahiya, Dr. Cengiz Satik and Professor Roland Horne. The aim of this project is to characterize boiling in homogeneous and fractured porous media.

## 2.1 INTRODUCTION

The process of boiling is necessarily linked to material and energy transport in geothermal systems. An understanding of boiling in a porous medium is valuable since it provides insights as to how, for instance, an initially liquid-filled reservoir changes into being vapor-dominated.

The boiling experiments in porous medium conducted by Dr. Cengiz Satik in 1997 will be extended to the case of a porous medium with a fracture. In the earlier experiments, a Berea sandstone core was used to observe vertical and horizontal boiling. The results of these experiments are currently being modeled numerically by Marilou Guerrero. A discussion of this effort can be found in Section 3 of this Report.

The research work described in this section extends the previous experiments to the case when a fracture exists in the porous medium. We shall conduct experiments once more on sandstone cores without a fracture, and introduce a fracture in the same core to conduct a second set of experiments. By using the same core, we are reducing the ambiguity in comparing results and investigating the effect of a highly conductive feature such as the fracture. We shall focus on investigating vertical boiling with heat originating from the bottom.

During the experiment we will apply heat to a water-saturated core and allow it to boil. Pressure, temperature and heat losses will be measured along the core to observe the expansion of the two-phase zone. The data will then be analyzed by numerical modeling in order to infer relative permeabilities for the porous medium and for the fracture.

## 2.2 EXPERIMENTAL SETUP AND METHOD

The porous medium to be used is a Berea sandstone core that is 17 inches in length and 2 inches in diameter. Typical permeability for such a sandstone is on the order of several hundred millidarcy. For the fracture experiment, an inner core will be cut from the 2-inch core to create an artificial fracture of radial symmetry. Figure 2.1(a) shows the core used in the original experiments. Figure 2.1(b) is an X-ray CT scan of the same core after a cylindrical fracture has been created by drilling a smaller radius core from the rock and replacing it into the resulting hole. The gap between the inner core and outer ring serves as fracture and is kept open by positioning spacers at both ends. We planned to use the original core for a fracture experiment and have reached a point where we were about to dry scan the core. However, the long history of the core and the epoxy enveloping it has

rendered it susceptible to thermal and mechanical stress. A crack developed along the outer core in the process of preparations for the experiment. Hence, we shall proceed with a different core.

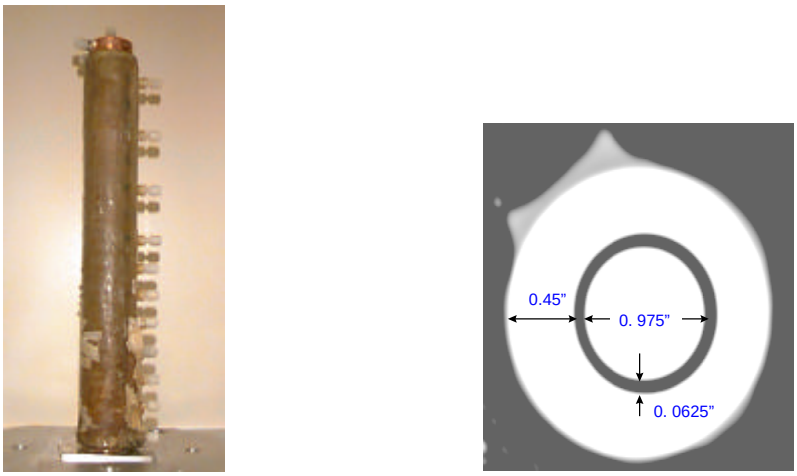


*Figure 2.1: (a) Original core used in past boiling experiments. (b) X-ray CT scan of the original core after creating a fracture.*

The experiments to be conducted will follow the methodology applied in last year's experiments. Briefly, the procedure is as illustrated in Figure 2.2 below. Core preparation involves securing the core using a coreholder. In the past, the core was covered with a thick layer of epoxy, which led to much difficulty in keeping the apparatus leak-free. This problem is addressed by the sturdier core holders that are now being used for the steady state relative permeability experiments described in Section 1. The core is sealed at both ends and evacuated with a vacuum pump while it is in an oven at gradually increasing temperatures of up to 120 $^{o}$C. The aim of this process is to dry the core as much as possible for purposes of obtaining a dry CT scan. Once the core has been scanned through the X-ray CT scanner, it is then fully saturated with water and once again scanned to obtain a wet profile. Average porosity is obtained from the difference of the wet and dry scans along the core length.

Figure 2.3 shows a schematic of the core assembly. The core is sealed at the top by a cooling pad and at the bottom by a copper end plate. Pressure ports through which thermocouples can be inserted line the core. The assembly is insulated to minimize heat losses. Heat flux sensors will also be placed on the surface of the core holder to measure actual loss of heat. The core sits on a base that houses the heating element. Actual input power will be measured by a heat flux sensor situated between the heater and the bottom end plate.

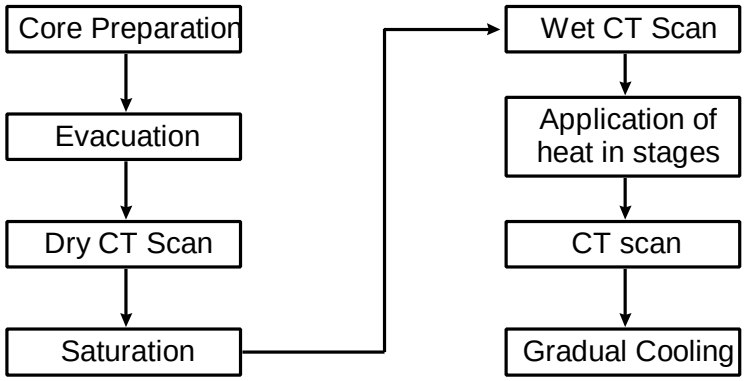


*Figure 2.2: General methodology for the boiling experiment*

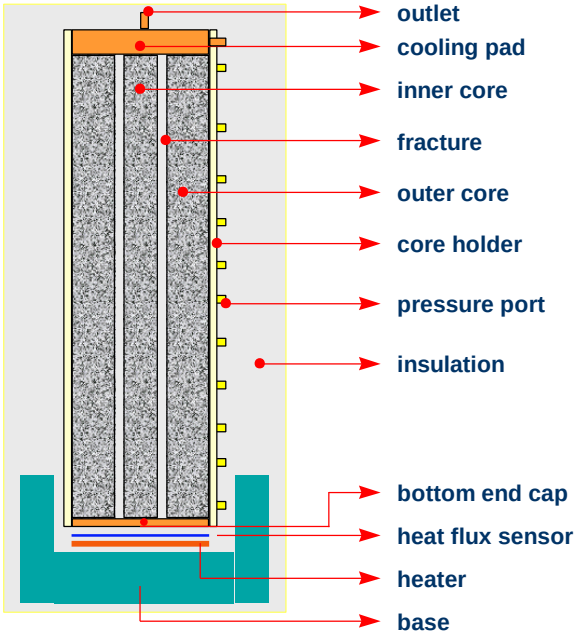


*Figure 2.3: Schematic of core assembly*

The main experiment is conducted by applying heat on the bottom of the core through a heater whose input power can be controlled. Starting from a low input power, the applied energy is increased in stages. Pressure, temperature and heat losses are continuously measured through thermocouples and heat flux sensors distributed along the core. These parameters are measured through transducers that interface with a data acquisition system, converting analog signals to digital information accessible through a computer. LABView, a graphical instrumentation software, will be used for real-time display of measurements.

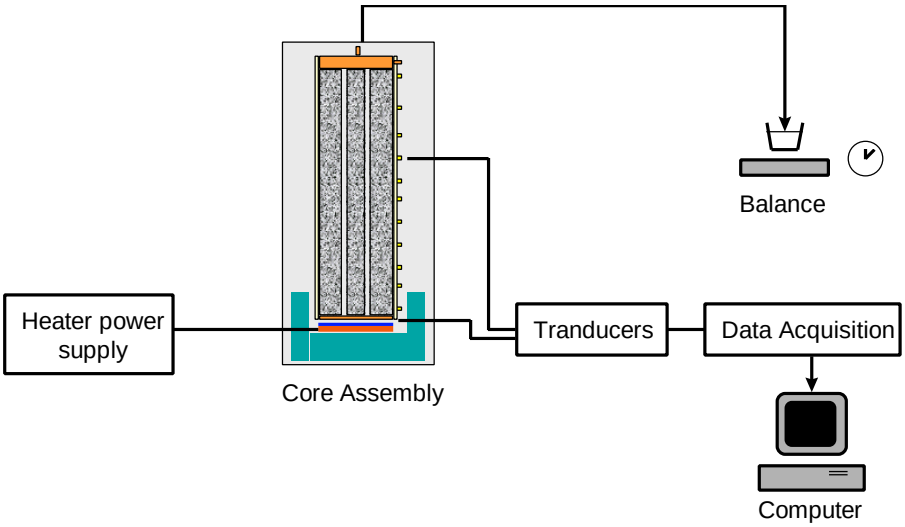


*Figure 2.4: Experimental setup for the vertical boiling experiment*

As heat is applied, water begins to boil and flow out of the core through the outlet at the top. The top is close to atmospheric pressure and held at constant temperature by flowing water through the cooling pad. The mass discharged from the core is measured with a balance and timer. Once a stable condition is reached for a given heater power setting, the core is run in the CT scanner to determine the variation of steam saturation with distance from the heat source. After this, the heater power is increased to the next setting. This process is repeated until the maximum design input power is reached. The core is then allowed to cool gradually.

## 2.3 NUMERICAL MODELING

The data obtained from the experiment will attempt to replicate the results through numerical simulation. TOUGH2 will be used for the forward calculations in which input parameters such as rock and thermal properties, heater power and estimated relative permeability and capillary pressure relations are given, and the pressure, temperature and heat fluxes are computed. Relative permeabilities are then altered until a reasonably close match between measured and simulated data is attained. This is the manner by which relative permeabilities are inferred. Another approach would be to employ inverse calculations facilitated by ITOUGH. In this case, the physical properties are used as the unknowns in this parameter estimation problem. Relative permeability functions will likewise be varied to obtain a match.

The current numerical model for the 1997 experiments has 51 layers along the axial direction and 4 concentric rings. The innermost ring represents the sandstone core, followed by a ring each of epoxy, insulation and the environment. A modification to this gridding will have to be made for the purpose of accommodating the fracture. Effectively, a group of rings will represent the inner core, one ring for the fracture, a group of rings for the outer core, and a ring each for the core holder and the environment.

## 2.4 FUTURE WORK

The next step in this project is to assemble a new core and conduct the experiment. Simulation runs will be made prior to the actual experiment in order to determine suitable heater power setting such that several steady states will be reached in the course of the study before the core dries out from heating. This will provide the opportunity to study sensitivity of the results to specific controllable parameters. Theoretical investigations will also be done to find analytic expressions for saturation distribution and the variation of mass flow rate for each phase along the core.

# 3. ESTIMATION OF RELATIVE PERMEABILITY FROM DYNAMIC BOILING EXPERIMENTS

This project is being conducted by Research Assistant Marilou Guerrero, with Dr. Cengiz Satik and Prof. Roland Horne from Stanford University, and in collaboration with Stefan Finsterle from the LBNL. The objective is to estimate relative permeability and capillary pressure by matching the measurements from a transient experiment to the results of a numerical simulation. The numerical model was constructed in TOUGH2 to simulate results taken from a vertical boiling experiment. Residual water saturation, $S_{wr}$, residual steam saturation, $S_{gr}$, pore size distribution index, $\lambda$, and gas entry pressure, $p_e$, were estimated for a Berea sandstone core by forward and inverse calculation using the Brooks-Corey relative permeability and capillary pressure functions.

## 3.1 INTRODUCTION

Recently, significant improvements were achieved in measuring saturation in steam-water relative permeability experiments (Ambusso, 1996). These results indicated a linear relationship for steam-water relative permeability. In attempting to repeat these results, Satik (1998) made improvements in the design of the experimental apparatus. A successful experiment was conducted and steam-water permeability was calculated. These recent results suggest a curvilinear relationship (i.e. Brooks-Corey type) that is different from the results obtained by Ambusso (linear relationship).

This project is taking a second approach to estimating the relative permeability by matching data from a transient boiling experiment to results obtained from numerical simulation. This method provides an independent way to examine the validity of the relative permeability measurements taken form the previous experiments as well as to estimate the capillary pressure.

## 3.2. EXPERIMENTAL APPARATUS

A 43-cm long Berea sandstone core that had a radius of 2.54 cm was used in the experiment. It was sealed with epoxy to prevent water from leaking on the sides, and it was wrapped in fiber blanket to minimize heat loss. The core was initially evacuated and then saturated with water. During the experiment (Fig. 3.1), the core was oriented vertically and heated from the bottom. To minimize heat loss from the heater, the heater was wrapped in fiberboard. Water was collected from the top of the core in a reservoir that was weighed on a scale. The experiment lasted for 169.5 hours, during which temperature, pressure, and heat flux measurements were taken at different locations on the core using thermocouples, pressure transducers, and heat flux sensors, respectively. At the same time, water saturation was measured using a CT scanner. A detailed description of this experiment was included in the July-September 1997 quarterly report.

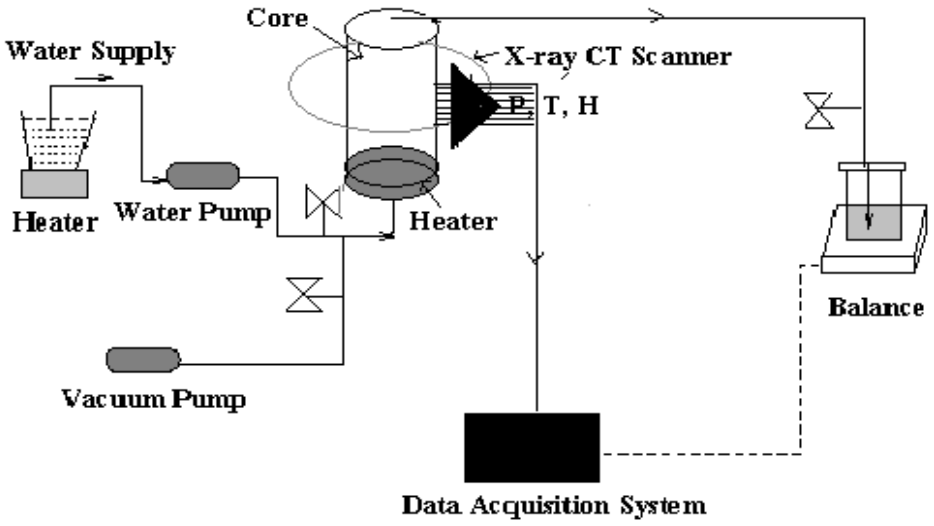


*Figure 3.1 Schematic diagram of the experimental apparatus (from Satik, 1997).*

## 3.3. BROOKS-COREY FUNCTIONS

The modified Brooks-Corey relative permeability functions are given as:

$$k_{rl} = S_{ek}^{(2-3\,l)/\,l} \tag{3.1}$$

$$k_{rg} = (1 - S_{ek})^2 (1 - S_{ek}^{(2-3\,l)/\,l}) \tag{3.2}$$

The modified Brooks-Corey capillary pressure functions are given as

$$p_c = -p_e \left[ e / (1 - S_{wr}) \right]^{-1/\,l} - (p_e /\ l) \left[ e / (1 - S_{wr})^{(1-\,l)/\,l} \right] (S_l - S_{wr} - e) \quad \text{for } S_l < (S_{wr} + e) \tag{3.3}$$

$$p_c = p_e (S_{ek})^{(2-3\,l)/\,l} \quad \text{for } S_l \geq (S_{wr} + e) \tag{3.4}$$

where

$$S_{ec} = (S_l - S_{wr}) / (1 - S_{wr}) \tag{3.5}$$

$$S_{ek} = (S_l - S_{wr}) / (1 - S_{wr} - S_{gr}) \tag{3.6}$$

and $S_l$ is the liquid saturation, $S_{wr}$ is the residual liquid saturation, $S_{gr}$ is the residual gas saturation, $\lambda$ is the pore size distribution index, and $p_e$ is the gas entry pressure. To prevent the capillary pressure from approaching infinity as the effective saturation goes to zero, a linear function is used for $S_l < (S_{lr} + \varepsilon)$, where $\varepsilon$ is a small number.

## 3.4. NUMERICAL SIMULATION

A model of the experiment was constructed in TOUGH2 (Fig. 3.2), a multidimensional numerical model for simulating the transport of water, steam, air, and heat in porous and fractured media (Pruess, 1991). Forward calculations were carried out to obtain the initial guesses for the parameters, and inverse calculations were carried out to estimate the different parameters using ITOUGH2. ITOUGH2 provides inverse modeling capabilities for the TOUGH2 codes and solves the inverse problem by the maximum likelihood approach (Finsterle et al, 1996). In this study, parameters were estimated based on temperature, pressure, steam saturation, and heat flux for which a corresponding TOUGH2 output was already available, including initial guesses for the parameters to be estimated.

### *Model*

The numerical model is a two-dimensional radial model with 3 concentric rings and 51 layers. Except for layers 46-51 (six bottommost layer), ring 1 (innermost ring) represents the core, ring 2 represents the epoxy, and ring 3 represents the core insulation material. The heater is in ring 1, layer 46, which is subdivided further into five layers. The heater insulation is in rings 1-3, layers 47-51. Rings 2-3 in layer 46 consist of epoxy and core insulation, respectively. Constant pressure boundary conditions are applied to ring 1, layer 1 to model liquid phase conditions on the top layer of the core during the entire experiment. A grid block under ambient conditions is attached to all grid blocks in ring 3 to simulate heat loss to the surroundings. To model constant pressure and ambient conditions, grid blocks associated with these conditions were assigned extremely large volumes. Since fluid flowed out only from the top of the core, core permeability in the radial direction was neglected.

### Forward Calculations

To obtain reasonable initial guesses for the Brooks-Corey two-phase parameters, measured relative permeability was matched with calculated relative permeability. By trial-and-error, a rough fit was obtained at $S_{wr}$=0.2, $S_{gr}$=0.1 and $\lambda$=2.5 (Fig. 3.3). The initial guess for $p_e$ was arbitrarily taken at 1000 Pa since the capillary pressure was still unknown.

### Inverse Calculations

Two methods of inverse calculation were employed to estimate the thermal conductivity of the sandstone, $\alpha_s$, thermal conductivity of the core insulation, $\alpha_i$, thermal conductivity of the heater insulation, $\alpha_b$, absolute permeability of the core, k, $S_{wr}$, $S_{gr}$, $\lambda$, and $p_e$. These two approaches will be referred to as the one-step and two-step methods.

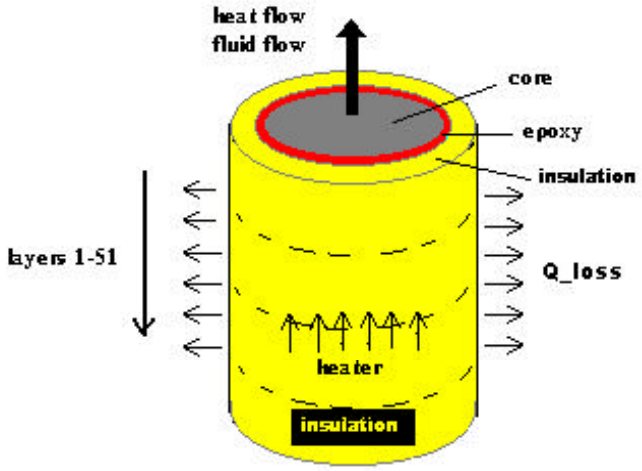


*Figure 3.2. The two-dimensional radial model of the vertical boiling experiment.*

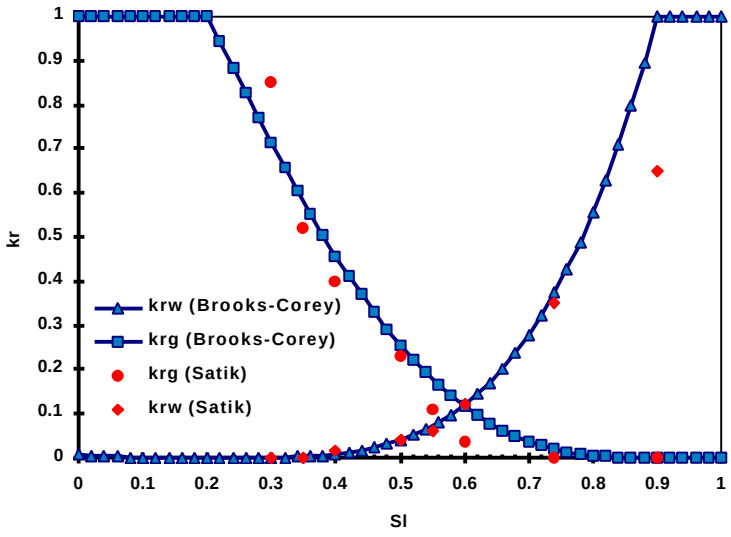


*Figure 3.3. Initial guesses for relative permeability parameters: $S_{wr}$=0.2, $S_{gr}$=0.1, and $l$=2.5.*

***One-step Method***

The one-step method involved simultaneous optimization of all the parameters using single-phase and two-phase data. In the plots shown here, the numbers indicate the temperature (T), pressure (P), heat flux (HF) and steam saturation (Sst) sensor locations, where Sensor 1 is closest to the heater and Sensor 4 is farthest from the heater. Except for

T1, there is a good fit between the measured and simulated temperature data at T2, T3, and T4 during single-phase flow (time<120 hours) (Fig 3.4). On the other hand, the simulated pressure data do not match the measured data, although the general behavior of the simulated data is similar to the trend of the measured data at P1 and P2 (Fig. 3.5). Similarly, the observed steam saturation data and simulated results do not appear to give a good fit primarily because steam saturation was measured only three times at every observation port (Fig. 3.6). Steam saturation data were interpolated between the measured points to generate data at calibration times when there were no observed data. These measured and interpolated data points were used during the calibration phase, when measured and simulated data were compared and the weighted difference between them was minimized. The observed and calculated data for heat flux give a good fit at HF2 and HF3 almost all throughout the experiment (Fig. 3.7). The relative permeability associated with the estimated values using one-step method is shown in Figure 3.8. However, the estimated values of $S_{wr}$, $S_{gr}$ and $\lambda$ yield a relative permeability to the right of the relative permeability generated from the initial guess, farther from their values based on the results obtained by Satik. The capillary pressure associated with the estimated parameters is shown in Figure 3.9. Table 3.1 shows a summary of the estimated parameter set employing the one-step inversion method.

The statistical measures associated with the parameters are given in Table 3.2. The standard deviation of the parameter estimate, $\sigma_p$, takes into account the uncertainty of the parameter itself and the influence from correlated parameters. The conditional standard deviation, $\sigma_p$*, reflects the uncertainty of one parameter if all the other parameters are known. Hence, $\sigma_p$*/$\sigma_p$ (column 3) is a measure of how independently a parameter can be estimated. A value close to one denotes an independent estimate, while a small value denotes strong correlation to other uncertain parameters. The total parameter sensitivity (column 4) is the sum of the absolute values of the sensitivity coefficients, weighted by the inverse of individual measurement errors and scaled by a parameter variation (Finsterle et al, 1997).

As shown in Table 3.2, $\sigma_i$ and $\sigma_b$ are the most sensitive parameters. All parameters cannot be determined independently because they are strongly correlated to one or more of the other parameters (column 3). Moreover, the relatively large standard deviation of the estimated values of $\lambda$ and $p_e$ is due to the fact that the capillary pressure is dependent on both $\lambda$ and $p_e$ (Equations 3.3 and 3.4).

Table 3.3 gives the statistical parameters related to the residuals. Comparing the total sensitivity (column 2) of the different observation types, accurate measurements of temperature, pressure, and steam saturation are sufficient to solve the inverse problem, i.e. heat flux data are much less sensitive. The standard deviation values of the final residual (column 3) are of the same order of magnitude as the measurement errors indicating that there are no significant systematic errors present. Lastly, the contribution of each observation type to the final value of the objective function (COF) is relatively evenly distributed suggesting that the choice of weighting factor is reasonable.

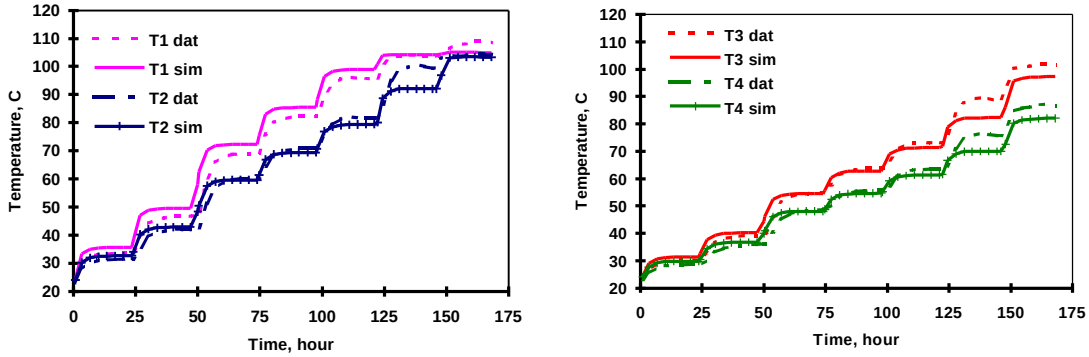


*Figure 3.4. One step method: temperature match at T1, T2, T3, and T4.*

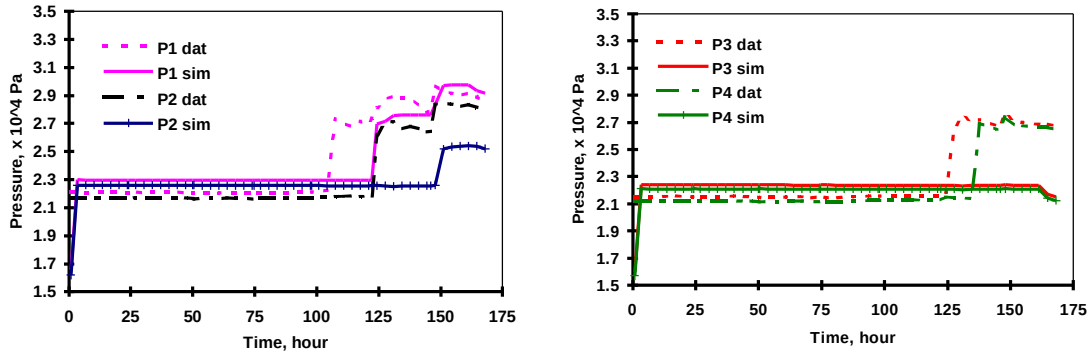


*Figure 3.5. One step method: pressure match at P1, P2, P3, and P4.*

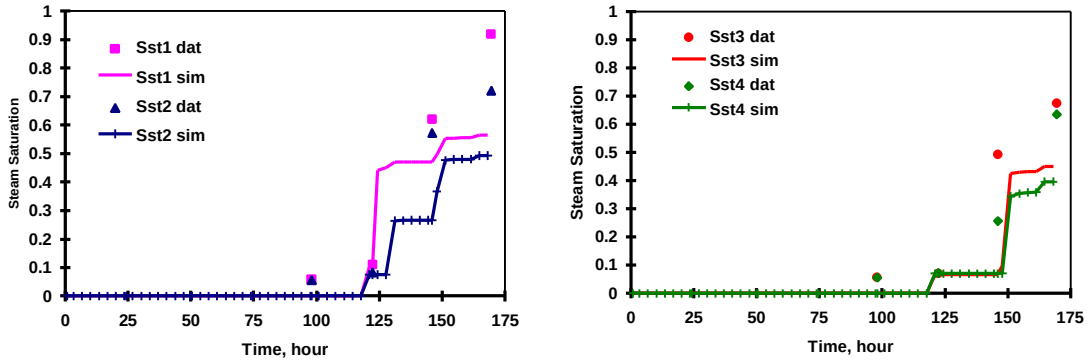


*Figure 3.6. One step method: steam saturation match at Sst1, Sst2, Ss3, and Sst4.*

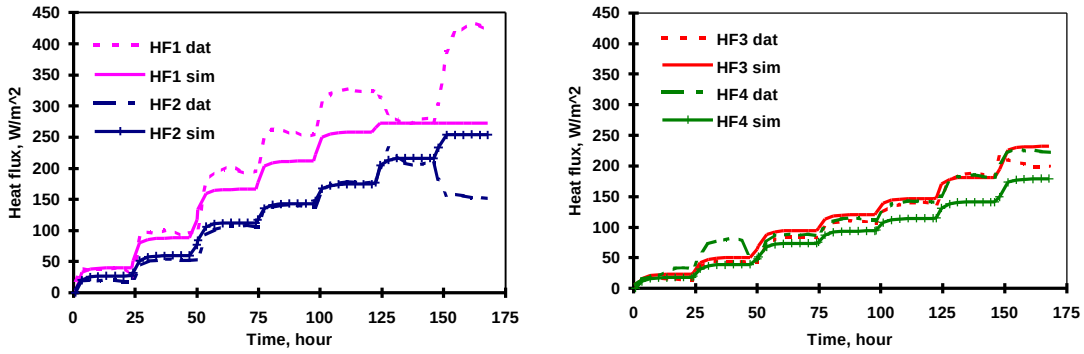


*Figure 3.7. One step method: heat flux match at HF1, HF2, HF3, and HF4.*

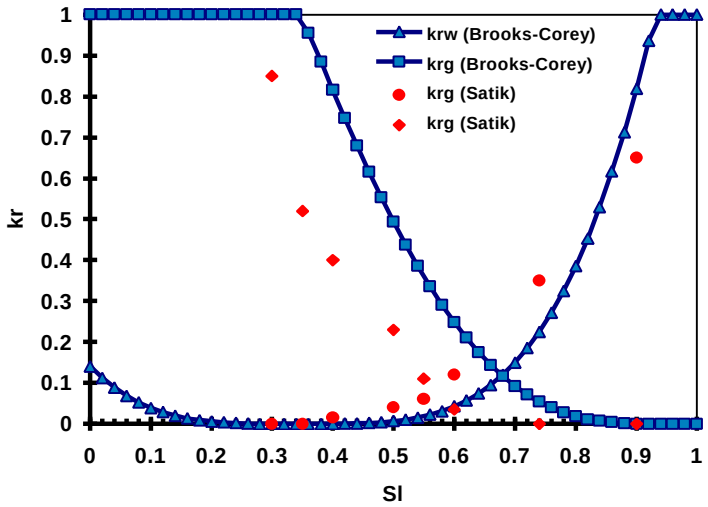


*Figure 3.8. One-step method: Brooks-Corey relative permeability.*

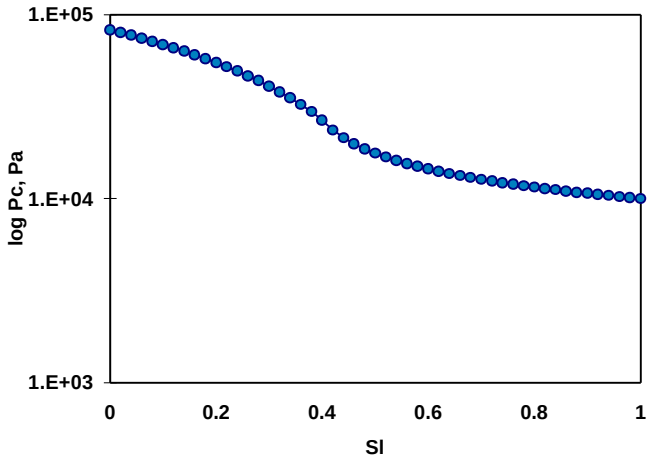


*Figure 3.9. One-step method: capillary pressure.*

*Table 3.1. One-step method: parameter initial guesses and best estimates.*

| Parameter | Initial Guess | Best Estimate |
|---|---|---|
| $\alpha_s$, W/m-C | 4.326 | 4.316 |
| $\alpha_i$, W/m-C | 0.090 | 0.109 |
| $\alpha_b$, W/m-C | 0.125 | 0.134 |
| log k, $m^2$ | -12.07 | -12.16 |
| $S_{wr}$ | 0.200 | 0.251 |
| $S_{gr}$ | 0.100 | 0.057 |
| $\lambda$ | 2.500 | 2.091 |
| log $p_e$, Pa | 3.00 | 3.827 |

*Table 3.2. One-step method: statistical measures and parameter sensitivity.*

| Parameter | $\sigma_p$ | $\sigma_p^*/\sigma_p$ | Parameter Sensitivity |
|---|---|---|---|
| $\alpha_s$ | 0.0508 | 0.3248 | 1858 |
| $\alpha_i$ | 0.0008 | 0.2500 | 182210 |
| $\alpha_b$ | 0.0041 | 0.1707 | 43218 |
| log k | 0.0190 | 0.2316 | 3246 |
| $S_{wr}$ | 0.0204 | 0.3774 | 2884 |
| $S_{gr}$ | 0.0266 | 0.4549 | 2239 |
| $\lambda$ | 0.4581 | 0.1465 | 362 |
| Log $p_e$ | 0.1015 | 0.1419 | 1764 |

*Table 3.3. One-step method: total sensitivity of observation, standard deviation of residuals, and contribution to the objective function (COF).*

| Observation | Sensitivity | Std Dev | COF % |
|---|---|---|---|
| Temperature | 1520 | 2.57 | 23.11 |
| Pressure | 1158 | 1430 | 16.25 |
| Saturation | 1340 | 0.113 | 41.10 |
| Heat flux | 281 | 26.8 | 19.43 |

***Two-step method***

The first step in the two-step parameter estimation method involved optimization of k, $\alpha_s$, $\alpha_i$, and $\alpha_b$ using single-phase data only. The model was calibrated only against temperature and heat flux since there were no pressure and saturation gradients in the single-phase region at the different measurement locations. Figures 3.10 and 3.11 show that the observed and simulated temperature data give a good fit at T2, T3 and T4, and

HF2, HF3 and HF4, respectively. However, the temperature residuals are large (~10$^{o}$ C) at the start of each heat flux change.

The second step in the two-step method involved optimization of $S_{wr}$, $S_{gr}$, $\lambda$, and $p_e$ using two-phase data and the estimated parameters obtained from the first step. Figures 3.12-3.15 show very similar results to Figures 3.4 –3.7, respectively. However, the associated relative permeability (Fig. 3.16) is better than the one obtained from the one-step method in that it is closer to the measured relative permeability. The corresponding capillary pressure is shown in Figure 3.17. Table 3.4 shows a summary of the estimated parameter set employing the two-step inversion method.

Table 3.5 shows that $S_{wr}$ and $S_{gr}$ can be measured independently in Step 2 as indicated by their high $\sigma_p^*/\sigma_p$ ratios. Moreover, $S_{gr}$ and $p_e$ are the most sensitive parameters (column 4). Comparing the total sensitivity (column 2) of the different observation types, accurate measurements of pressure and steam saturation are sufficient to solve the inverse problem in Step 2. The standard deviation values of the final residual (column 3) are of the same order of magnitude as the measurement errors indicating that there are no significant systematic errors present.

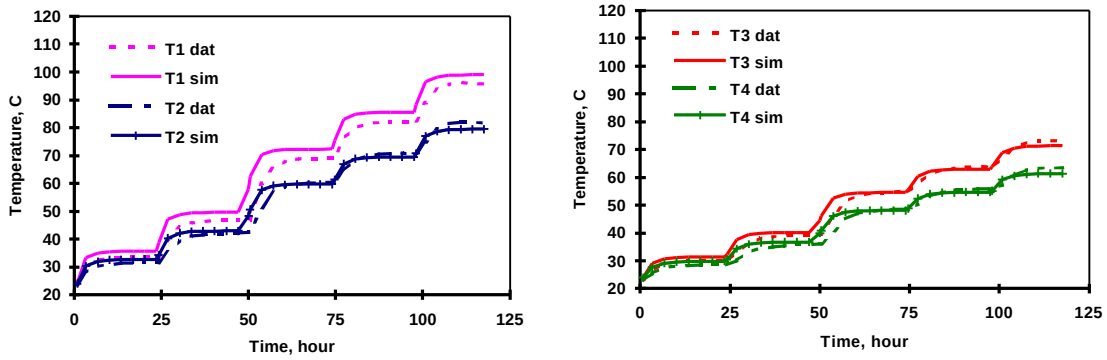


*Figure 3.10. Two-step method: Step 1 temperature match at T1, T2, T3, and T4.*

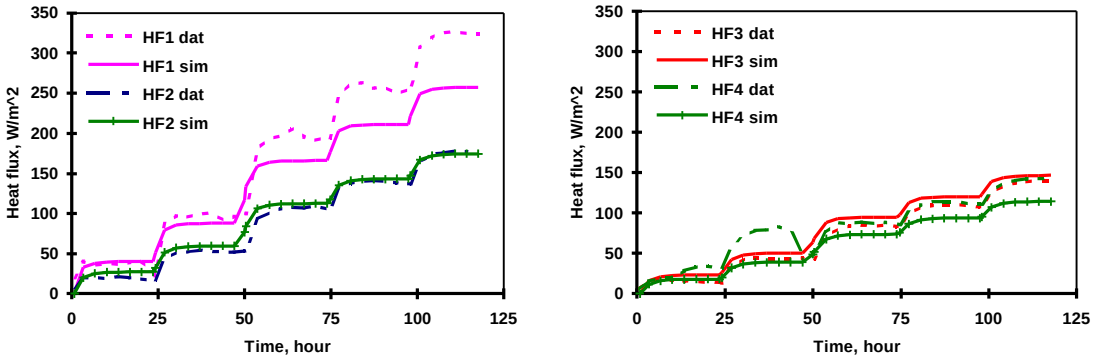


*Figure 3.11. Two-step method: Step 1 heat flux match at HF1, HF2, HF3, and HF4.*

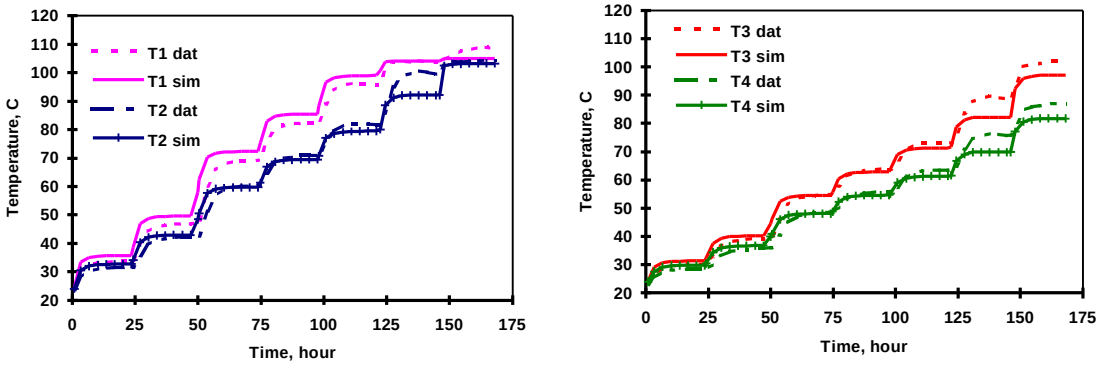


*Figure 3.12. Two-step method: Step 2 temperature match at T1, T2, T3, and T4.*

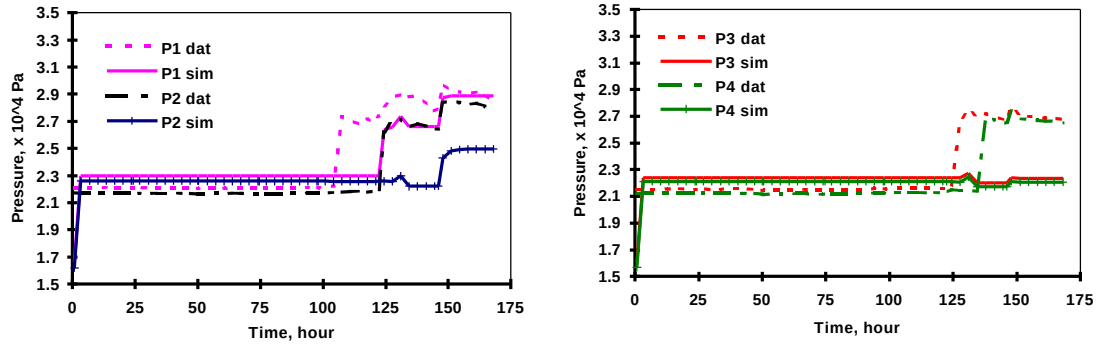


*Figure 3.13. Two-step method: Step 2 pressure match at P1, P2, P3, and P4..*

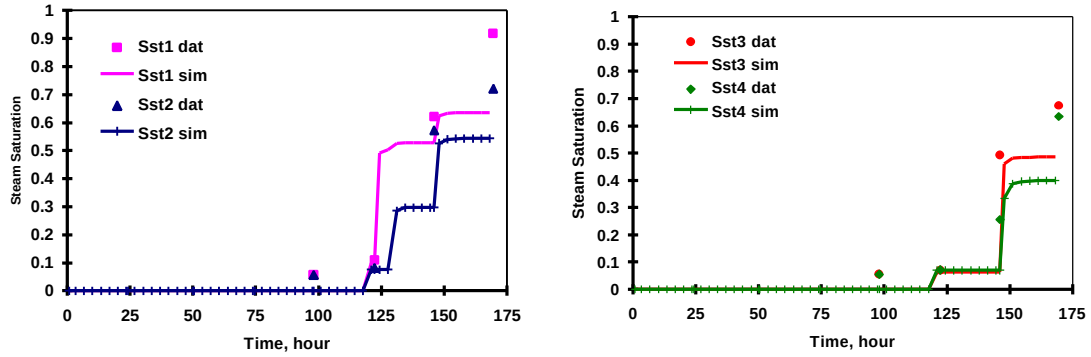


*Figure 3.14. Two-step method: Step 2 steam saturation match at Sst1, Sst2, Sst3, and Sst4.*

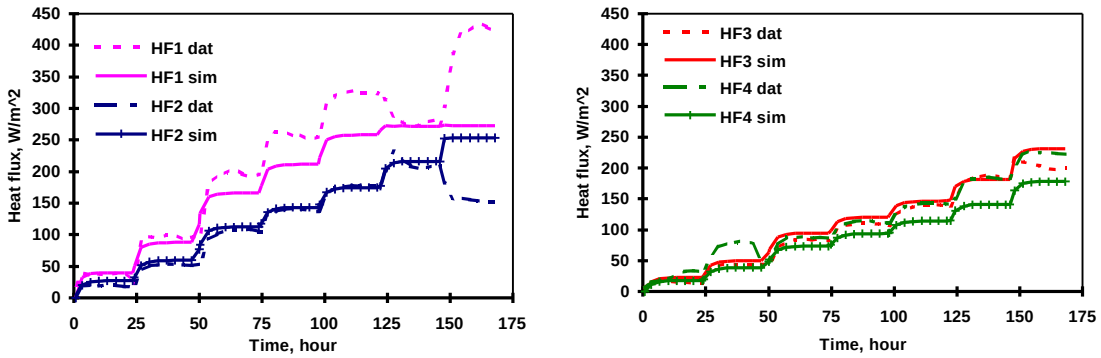


*Figure 3.15. Two-step method: Step 2 heat flux match at HF1, HF2, HF3, and HF4.*

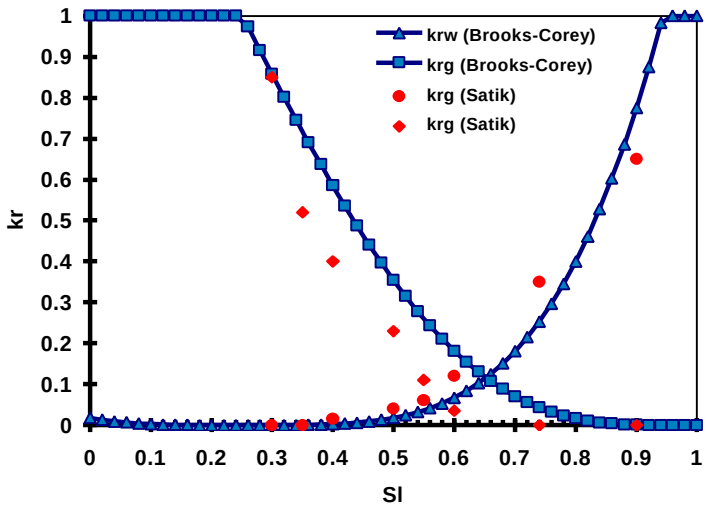


*Figure 3.16. Two-step method: Brooks-Corey relative permeability.*

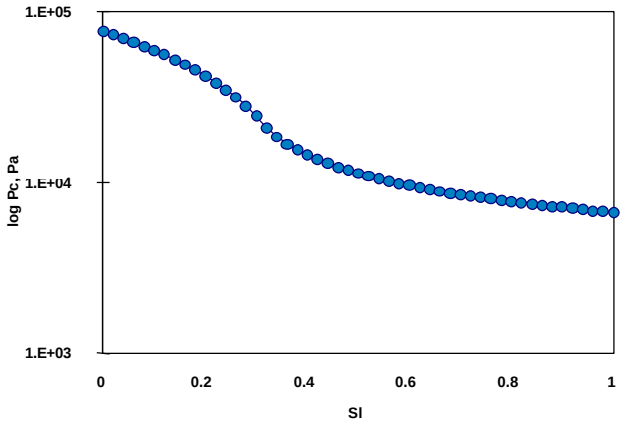


*Figure 3.17. Two-step method: Brooks-Corey capillary pressure.*

*Table 3.4. Two-step method: initial guesses and best estimates for parameters..*

| Parameter | Initial Guess | Best Estimate |
|---|---|---|
| $\alpha_s$, W/m-C | 4.316 | 4.366 |
| $\alpha_i$, W/m-C | 0.109 | 0.101 |
| $\alpha_b$, W/m-C | 0.134 | 0.152 |
| log k, $m^2$ | -12.16 | -12.38 |
| $S_{wr}$ | 0.200 | 0.347 |
| $S_{gr}$ | 0.100 | 0.070 |
| $\lambda$ | 2.500 | 2.556 |
| log $p_e$, Pa | 3.00 | 4.00 |

*Table 3.5. Two-step method: statistical measures and parameter sensitivity.*

| Parameter | $\sigma_p$ | $\sigma_p^*/\sigma_p$ | Parameter Sensitivity |
|---|---|---|---|
| $S_{wr}$ | 0.0861 | 0.9852 | 188 |
| $S_{gr}$ | 0.0109 | 0.9097 | 8312 |
| $\lambda$ | 0.0833 | 0.4484 | 422 |
| log $p_e$ | 0.1812 | 0.4411 | 3319 |

*Table 3.6. Two-step method: total sensitivity of observation, standard deviation of residuals, and contribution to the objective function (COF).*

| Observation | Sensitivity | Std Dev | COF % |
|---|---|---|---|
| Temperature | 81 | 2.95 | 18.75 |
| Pressure | 769 | 2320 | 14.92 |
| Saturation | 1258 | 0.129 | 58.35 |
| Heat flux | 19 | 12.0 | 7.95 |

## 3.5 SUMMARY

To summarize, a model was constructed in TOUGH2, and forward and inverse calculations were carried out using ITOUGH2. However, $S_{wr}$, $S_{gr}$, and $\lambda$ are still to be estimated more accurately. This can be achieved more easily if $p_e$ is known. Another vertical boiling experiment is being used to estimate the two-phase parameters employing the same methods that were discussed in this report.

# 4. APPLICATION OF X-RAY CAT SCAN IN POROSITY AND SATURATION MEASUREMENT

This project is being conducted by Research Assistant Meiqing He, Dr. Cengiz Satik and Professor Roland Horne. The aim of this project is to identify and to characterize fractures in geothermal rocks using X-ray computer tomography (CT). The porosity and saturation calculation processes are closely related to fracture calibration. In earlier reports, we discussed the fundamental physics of the CT technique and proposed two ways of porosity and saturation calculation. We proposed a denoising method, soft-thresholding the coefficients of wavelet transform, as a preprocess prior to edge detection in CT images of Geysers' core. We also applied the edge detection algorithm to CT image of Geysers core. In this report we present the Hough transform to detect the line features in core CT images and the Active Contour Model for finding the connected contour of the fracture. A general procedure of determining fracture aperture is proposed.

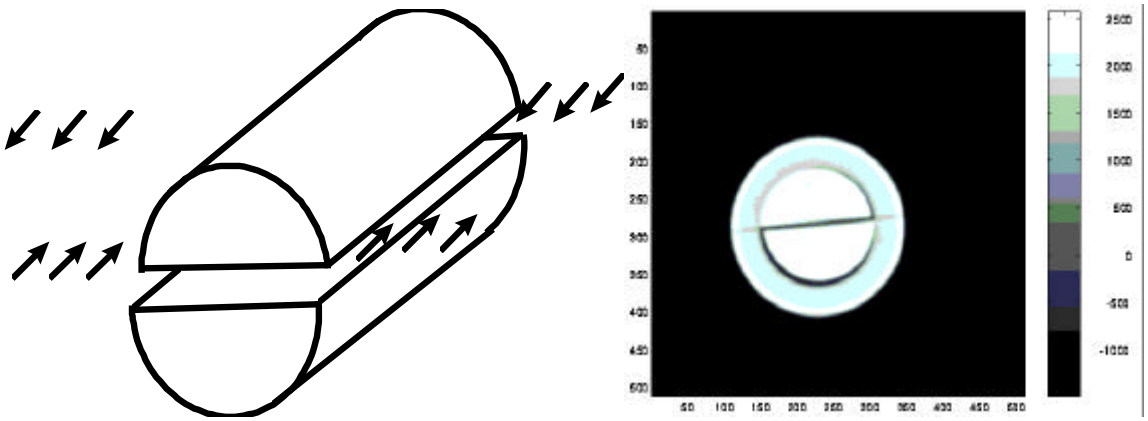

*(a)* *(b)*

*Figure 4.1 (a) Experimental setup. (b) CT image of (a).*

## 4.1 CALIBRATION EXPERIMENT

In the last quarterly report we discussed the dispersion effect inherent in the CT scanner and the existance of a linear relationship between the fracture aperture size and the integrated missing CT number over the gap (Johns, 1991). In order to calibrate this curve an experiment was performed. The experimental apparatus is illustrated in Figure 4.1(a). A Basalt core was used because of its homogeneity. The original basalt core was 4.5 cm in diameter and 8 cm in length. The core was cut in half and both planar surfaces were optically polished. The smoothness of the surfaces was 0.5 micron. Two shim stocks having calibrated thickness were inserted from both ends of the core along the direction of the arrows and an artificial fracture was created. The range of fracture size was 0.001~0.04 inch. An aluminum ring surrounded the basalt core in order to reduce the X-ray beam hardening effect. The calibration experiment should be done in a material with a distinctive density value within which the fracture will appear.

## 4.2 THEORETICAL DISCUSSION

### 4.2.1 Hough transform

The Hough transform can detect specific structural relationships between pixels in an image. The transform was proposed by Hough in 1962. Commonly, we use this approach to find subsets of given *n* points in an image that lie on straight lines (Pratt, 1991).

A line can be represented as

$$x\cos q + y\sin q = r \tag{4.1}$$

The meaning of the parameters used in Eq. (4.1) is illustrated in Figure 4.2(a). The Hough transform subdivides the parameter space into accumulator cells shown in Figure 4.1(b).

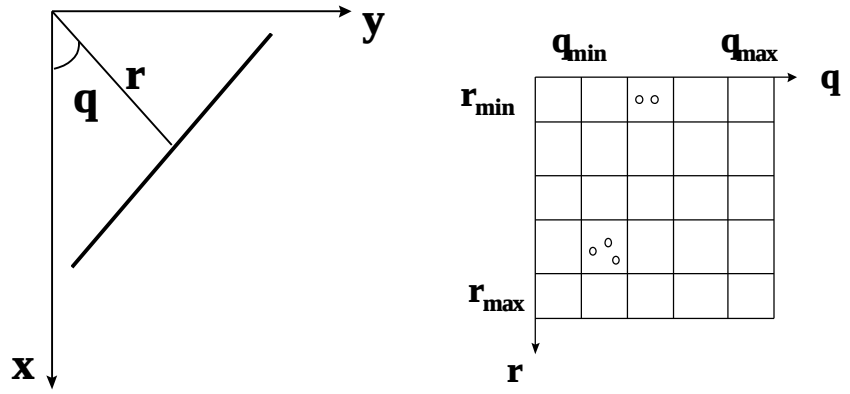


*(a)* *(b)*

*Figure 4.2(a) Normal representation of a line. (b) Quantization of $rq$ plane into cells*

The cell at coordinate (i, j) in the quantized ρθ plane, with accumulator value A(i, j), corresponds to a square associated with parameter space coordinates ($\rho_i$, $\theta_j$). Initially, these cells are set to zero. Then, for every point ($x_k$, $y_k$) in the image plane, we let parameter θ equal each of the allowed subdivision values on the θ axis and solve for the corresponding ρ using Eq. (4.1). The resulting ρ values are then rounded off to the nearest allowed value in the ρ axis. Therefore M collinear points lying on a line with parameter pair ($\rho_i$, $\theta_j$) will yield M sinusoidal curves that intersect at ($\rho_i$, $\theta_j$) in the parameter space, i.e. A(i, j) = M.

### 4.2.2 Active Contour Model

The Active Contour approach is an energy-minimizing model (Kass, Witkin and Terzopoulos, 1987). Because of the dynamic behavior of the approach, the curve is often referred to as a snake. A snake is an energy-minimizing spline regulated by internal forces, image forces and constraint forces. The energy of snake can be represented as

$$E^*_{snake} = \int \left[ E_{\text{int}}(v(s)) + E_{image}(v(s)) + E_{cont}(v(s)) \right] ds \tag{4.2}$$

Where $v(s) = (x(s), y(s))$ represents the position of snake parametrically. $E_{int}$ represents the controlled continuity spline forces which impose a piecewise smoothness constraint. The constraint can be written

$$E_{\text{int}} = \left(a(s)|v_s(s)|^2 + b(s)|v_{ss}(s)|^2\right)/2 \tag{4.3}$$

The first-order term makes the snake act like a membrane and the second-order term makes it act like a thin plate. $a(s)$ and $b(s)$ are the weights of the two terms. $E_{image}$ represents the image forces. Here we set

$$E_{image} = -|\nabla I(x, y)|^2 \tag{4.4}$$

In this way snake is attracted to large image gradients.

Minimizing the energy function (4.2) gives rise to the Euler equation in finite difference form, Eq. (4.7). Let

$$f_x(i) = \P E_{ext} / \P x_i \tag{4.5}$$

$$f_y(i) = \P E_{ext} / \P y_i \tag{4.6}$$

$$\begin{aligned} &a_i(v_i - v_{i-1}) - a_{i+1}(v_{i+1} - v_i) + b_{i-1}(v_{i-2} - 2v_{i-1} + v_i) - 2b_i(v_{i-1} - 2v_i + v_{i+1}) \\ &+ b_{i+1}(v_i - 2v_{i+1} + v_{i+2}) + (f_x(i), f_y(i)) = 0 \end{aligned} \tag{4.7}$$

Eq. (4.7) can be reorganized into matrix form.

$$Ax + f_x(x, y) = 0 \tag{4.8}$$

$$Ay + f_y(x, y) = 0 \tag{4.9}$$

where A is a pentadiagonal banded matrix. Equations (4.8) and (4.9) are solved using an explicit Euler method with respect to the external forces. The resulting equations are:

$$Ax^t + f_x(x^{t-1}, y^{t-1}) = -t(x^t - x^{t-1}) \tag{4.10}$$

$$Ay^t + f_y(x^{t-1}, y^{t-1}) = -t(y^t - y^{t-1}) \tag{4.11}$$

where $t$ is the step size. At equilibrium, the time derivative vanishes and a stable solution is obtained. Equations (4.10) and (4.11) can be solved by matrix inversion resulting in

$$x^t = (A + tI)^{-1}(x^{t-1} - f_x(x^{t-1}, y^{t-1})) \tag{4.12}$$

$$y^t = (A + tI)^{-1}(y^{t-1} - f_y(x^{t-1}, y^{t-1})) \tag{4.13}$$

## 4.3 RESULTS

### 4.3.1 Calibration

In the two-dimensional density image, a fracture is shown as a dark region. Figure 4.3(b) is the CT image of basalt core having an artificial fracture and surrounded by an aluminum ring. From the line profile of the CT number shown in Figure 4.3(a), we can tell the existence of a fracture by the valley in the profile. In Figure 4.3(a), the valley in the middle corresponds to the artificial fracture in the basalt core in Figure 4.3(b). Dispersion of the CT response is caused by the finite beam width and oversampling. Usually dispersion can appear within four to nine voxels surrounding the voxel in which the point is located. Also

if the voxel contains more than one component, the resulting attenuation response is determined by the volume fraction of each component and the attenuation response for each pure component. The integrated missing mass (CT number) corresponds linearly to the gap size. However we need to identify the starting and ending point of the integration. In Figure 4.3(b), two parallel lines emphasize the boundary of the fracture. Their positions were obtained by using the Hough transform discussed in Section 4.2. A line perpendicular to the fracture was obtained subsequently. The calculated integrated CT number over the gap was determined by fitting a straight line using the least square error method. The result is shown in Figure 4.4.

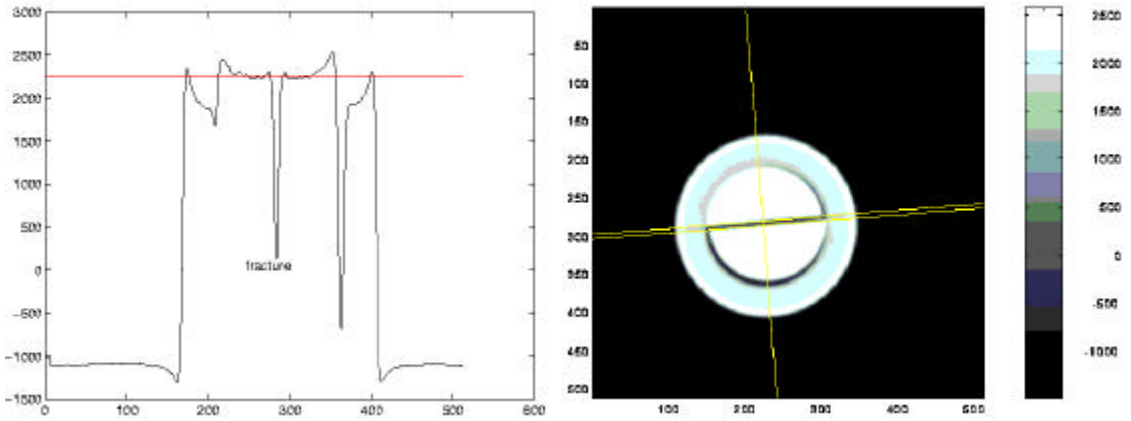


*(a)* *(b)*

*Figure 4.3 (a) CT number profile along the line perpendicular to fracture in (b). (b) CT image of basalt core with artificial fracture*

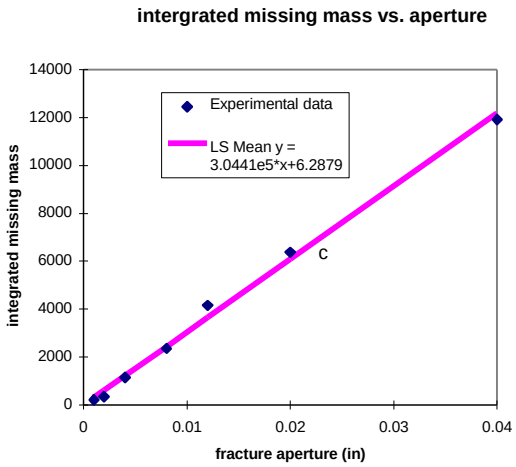


*Figure 4.4 Integrated missing CT number vs. fracture aperture*

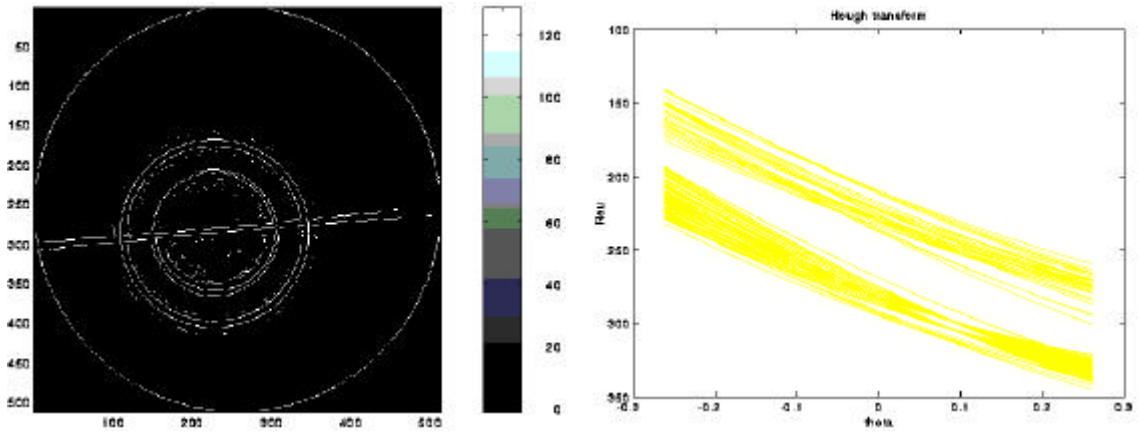


*(a)* *(b)*

*Figure 4.5 (a) Edge map of basalt core in calibration experiment. (b) Hough transform of the edge map. Two intersects are distinguished,* $r_1 = 303.6699 \quad q_1 = 0.0754$ $r_2 = 297.6210 \quad q_2 = 0.0843$

### 4.3.2 Hough transform

Figure 4.5 demonstrates how two straight lines are detected by the Hough transform. The two straight lines are drawn in Figure 4.3(b). These two lines correctly indicate the location of the boundary of the artificial fracture in basalt core.

### 4.3.3 Active contour model

The active contour method described in Section 4.2.2 was applied to the artificial fracture in the basalt core. Figure 4.6 shows the moving path of the snake during evolution. The correct contour was obtained at equilibrium.

Figure 4.7 demonstrates the problem with starting the snake close to edge points further from the object of interest. The snake was attracted by edges from objects other than the one under study. Therefore we have to push the snake closer to the object of interest in order to let the snake find the right path.

## 4.4 CONCLUSION

A general procedure for determining fracture aperture has been developed. The procedure includes the following steps:

(1) The experimental calibration of a curve of integrated missing mass vs. aperture using homogeneous material having similar density to the natural fractured core.

(2) Edge detection on the natural fractured core. A denoising procedure may be applied prior to edge detection.

(3) The active contour algorithm is used to refine the edge map.

(4) A heuristic graph search uses the information derived from the Hough transform and Active Contour methods to link the edge. Components are labeled if necessary.

(5) The identified fracture orientation is estimated using a local Hough transform. The fracture aperture size is interpreted based on curve of integrated missing CT number vs. fracture aperture obtained from the calibration experiment. The saturation of fluid in the fracture region can also be estimated.

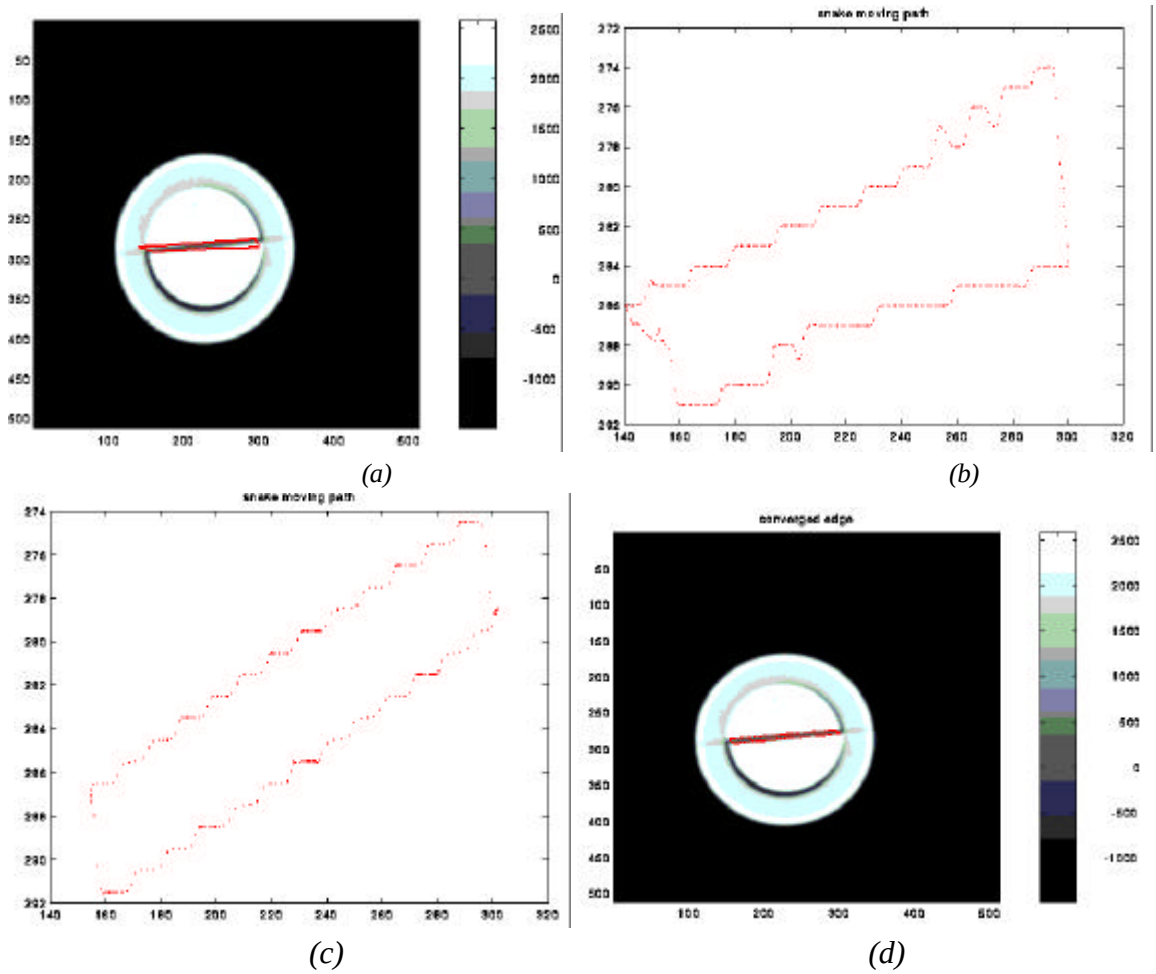


*(a)* *(b)* *(c)* *(d)*

*Figure 4.6 (a) Initial contour of fracture. (b) Locus of snake after one iteration. (c) Stable locus of snake after 300 iterations. (d) Final contour of fracture*

## 4.5 FUTURE WORK

The next stage of the project will consider two steps:

(1) Apply the Hough transform and the Active Contour approach to a sample of Geysers core.

(2) Calculate the fracture aperture in naturally-fractured core based on the calibrated curve of integrated missing CT number and aperture. Calculate the saturation inside of the fracture.

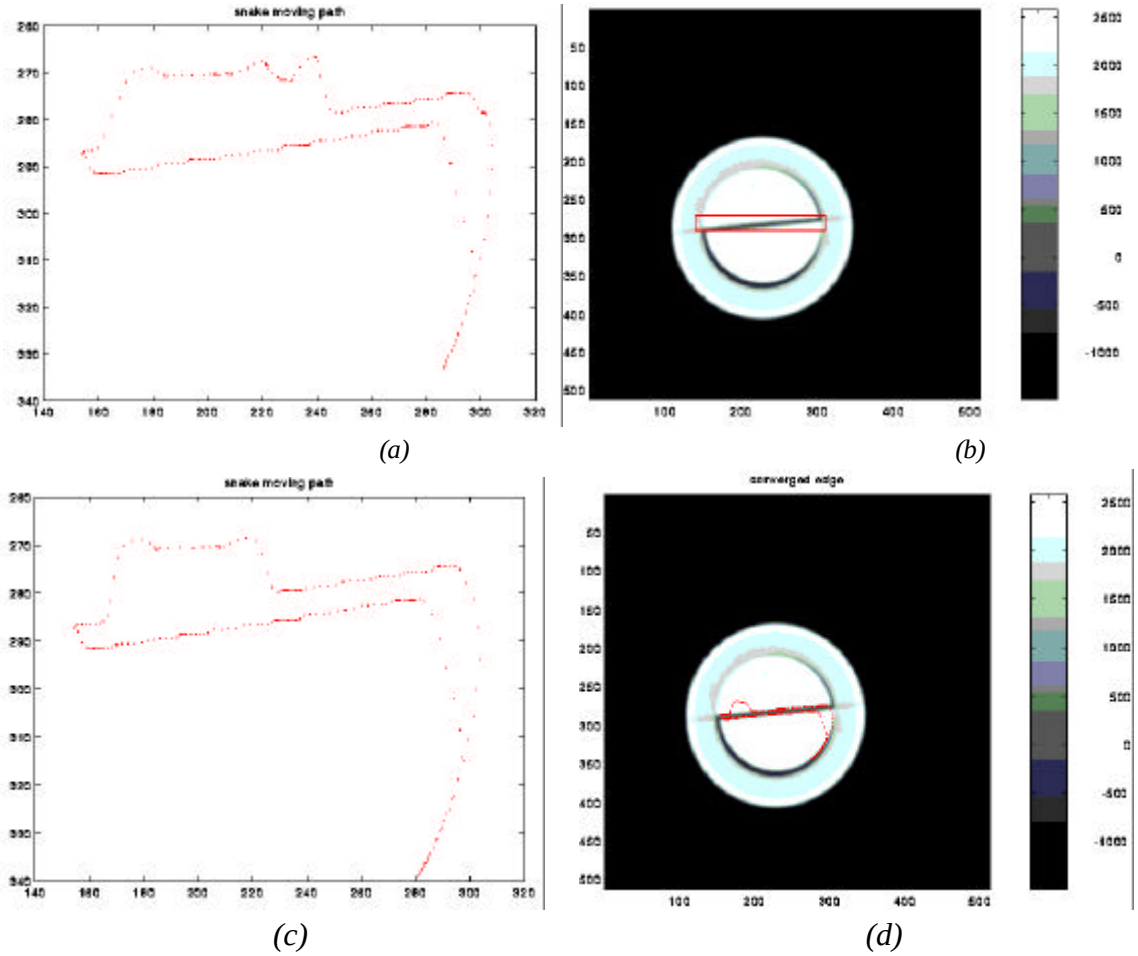


*(a)* *(b)*

*(c)* *(d)*

*Figure 4.7 Case study of setting initial contour not close enough to object of interest. (a) Initial contour of fracture. (b) Locus of snake after one iteration. (c) Stable locus of snake after 300 iterations. (d) Final contour of fracture*

# 5. BOILING IN A VERTICAL FRACTURE

This experimental study of boiling in an artificial fracture is being conducted by Research Assistant Bob DuTeaux, Dr. Cengiz Satik and Professor Roland Horne. The study has the goal of understanding fluid flow and heat transfer as liquid water flashes to steam in a fracture. A more thorough observational analysis of flow regimes and liquid-vapor phase transition has emerged, and a strategy for modeling is being developed. This strategy has involved the identification of flow and boiling regimes and the important fluid properties and parameters that control the convection of heat. Over the past quarter another transient experiment was run and a video tape of the boiling flow was recorded. In addition, a new apparatus was developed to examine nucleate boiling on the surfaces of sandstone and real geothermal rock (Geysers core). This apparatus was built to quantify the heat flux to a fracture surface during boiling as a function of the rock surface temperature, and to identify significant differences between boiling flow between glass surfaces and boiling flow on real rock surfaces.

## 5.1 THE INTERACTION OF FORCES

Observation of experiments has led to a better understanding of how the interaction of pressure, viscosity, inertia, gravity, and interfacial tension influence the mechanics of two-phase flow in a fracture. These forces have been grouped into dimensionless ratios along with fluid properties, and an effort to analyze the circumstances where they become important has begun. A dimensionless coefficient for convection, or Nusselt number, Nu, that relates heat flux to surface temperature in a fracture, has been considered a potential function of rock temperature above the fluid saturation temperature, $\Delta T_e$, Reynolds number, Re, Prandtl number, Pr, Jacob number, Ja, Bond number, Bo, Weber number, We, and fracture orientation with respect to gravity $\phi$. In multiphase heat exchange literature, empirical equations have been proposed to describe the convective boiling process in tubes and channels, and these relations have used a few or more of these dimensionless groups. Most important are the liquid and vapor Reynolds number, which compares the ratio of inertia to viscous forces, the Bond number, which is the ratio of gravity to interfacial tension, and the Weber number, which is the ratio of inertia to interfacial tension. Observation of transient experiments has led to the analysis of these dimensionless groups, and to the analysis of boiling and flow regimes.

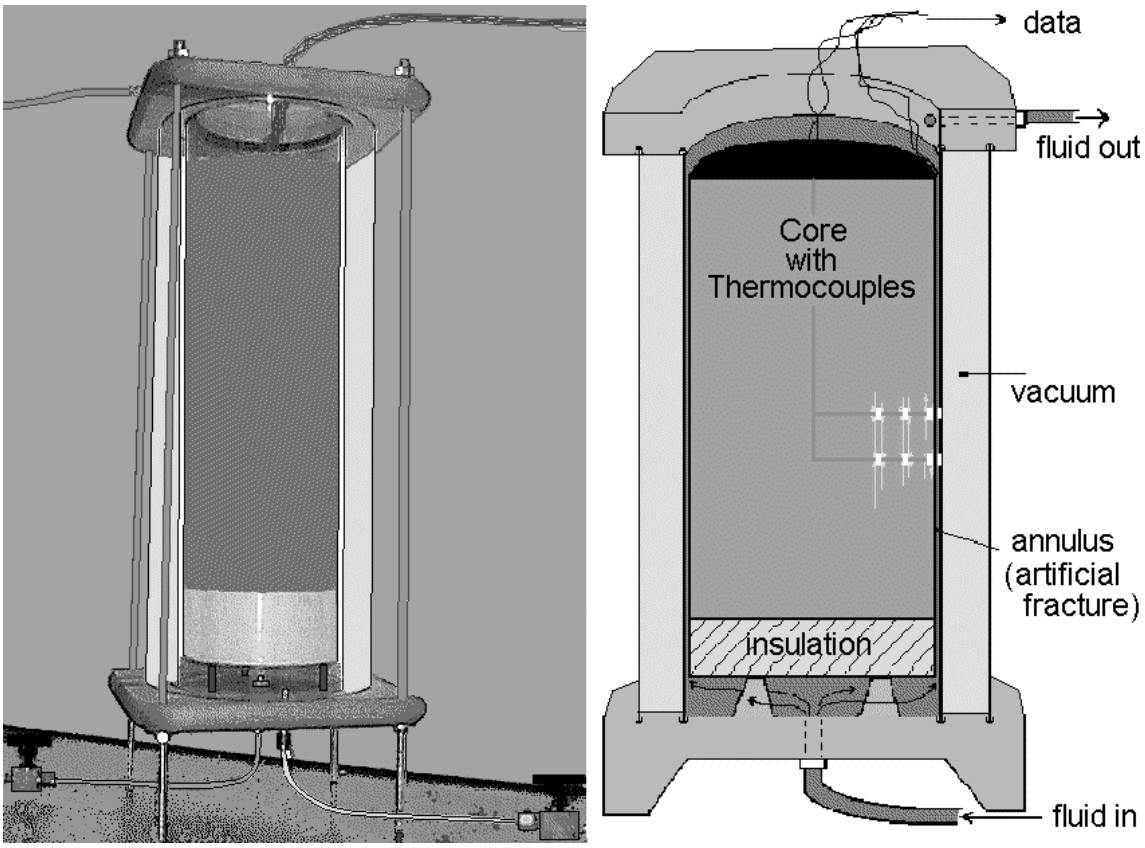


*Figure 5.1: Illustration of transient boiling experimental apparatus.*

### 5.1.1 Transient Experiment

The experimental apparatus illustrated in Figure 5.1 was constructed to measure the heat exchanged between an impermeable core and water flowing upward and boiling in the concentric annulus surrounding the core. The annulus between two large diameter glass tubes creates an artificial fracture less than 1.0 mm wide. The core is a 135 mm diameter glass cylinder, closed at the bottom to hold sand that has been heated to a temperature of about 150 $^{o}$C. Water flows on the outside of the glass core, not in the sand. The sand only provides a medium with a conductivity and heat capacity whose order of magnitude is comparable to real rock.

The apparatus is about 0.6 meters tall and has thermocouples attached to the inside and outside of the core. Heat flux sensors were also attached to the outside of the core. Another concentric cylinder surrounds the artificial fracture aperture to reduce radial heat loss by applying a vacuum. In a typical experiment, water was injected near atmospheric pressure from the bottom ($z = 0$) at a slow rate, so that (without boiling) it would take a few minutes to reach the top. With boiling, a two-phase flow quickly extended from the base to the top of the apparatus when flow reached the base of the fracture. Data from an experiment done in March is shown in Figures 5.2, 5.3, and 5.4.

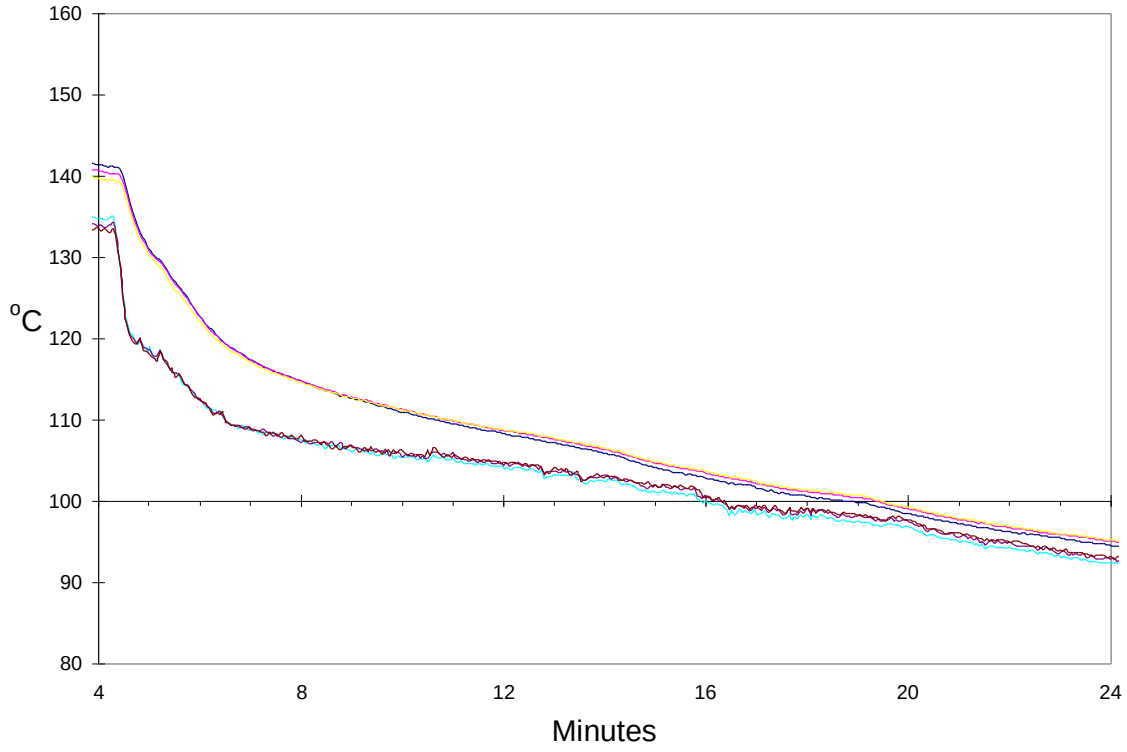


*Figure 5.2: Temperature data from transient boiling experiment.*

## 5.1.2 Data

Figure 5.2 shows the temperature decline in time measured with thermocouples placed on the glass surface adjacent to the boiling flow, and on the inner surface (radial inward) of the 3 mm thick glass. The higher temperatures were measured on the inner surface and the lower and more variable temperatures were measured adjacent to the flow. These temperature profiles have segments with distinctly different slopes that have been interpreted as time intervals dominated by a single boiling flow regime. In the initial steep temperature decline at a surface temperature from about $20^{o}$ above the saturation temperature (100 $^{o}$C), to about $10^{o}$ excess temperature some erratic temperature variations were recorded. These variations are reflected in the heat fluxes plotted in Figure 5.3. Additionally, Figure 5.2 indicates a relatively linear temperature decline from $10^{o}$ excess temperature down to the saturation temperature.

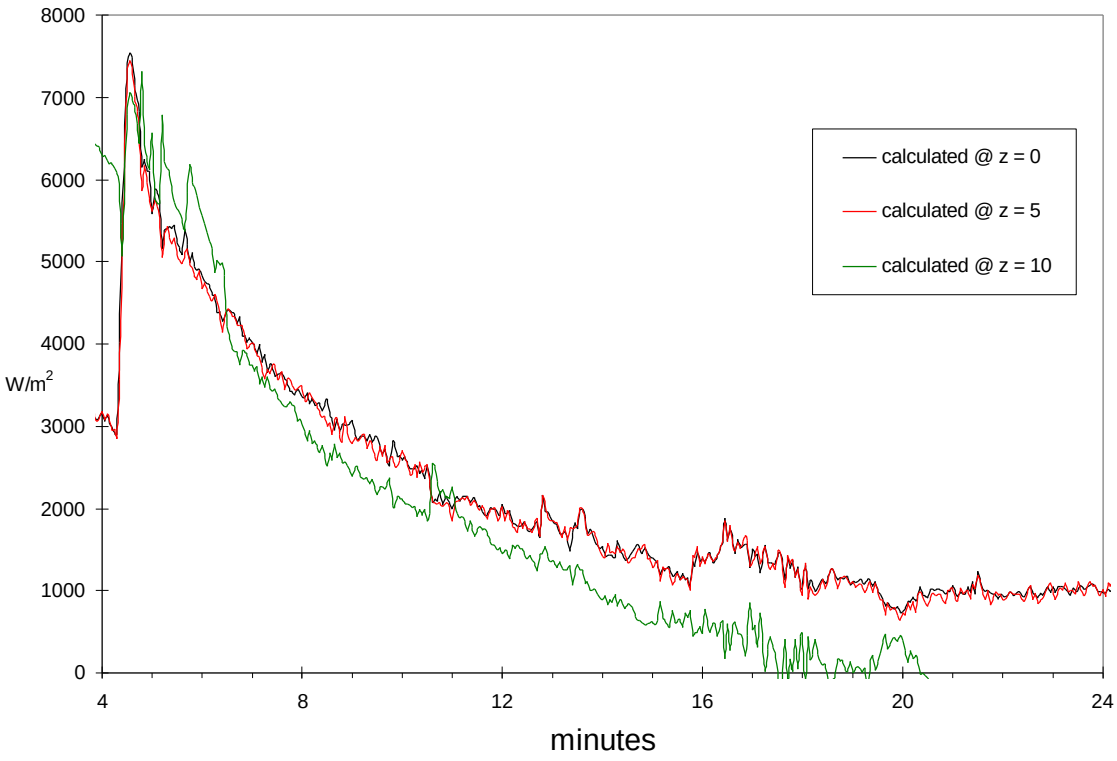


*Figure 5.3: Heat fluxes calculated from thermocouples separated by 3mm of glass.*

The magnitude of maximum heat flux recorded was a brief transient near 7000 W/m$^2$ when fluid first entered the fracture and then declined to about 1000 W/m$^2$ as the boiling surface declined to saturation temperature at about 16 minutes. It is believed that a similar transient heat flux could occur as water is injected into a superheated fracture, but because the surfaces of real rocks are porous and somewhat permeable, it is unknown if the magnitude of the heat flux could be much greater. Again there seem to be distinct segments that could be interpreted as indications of boiling regimes and flow regimes.

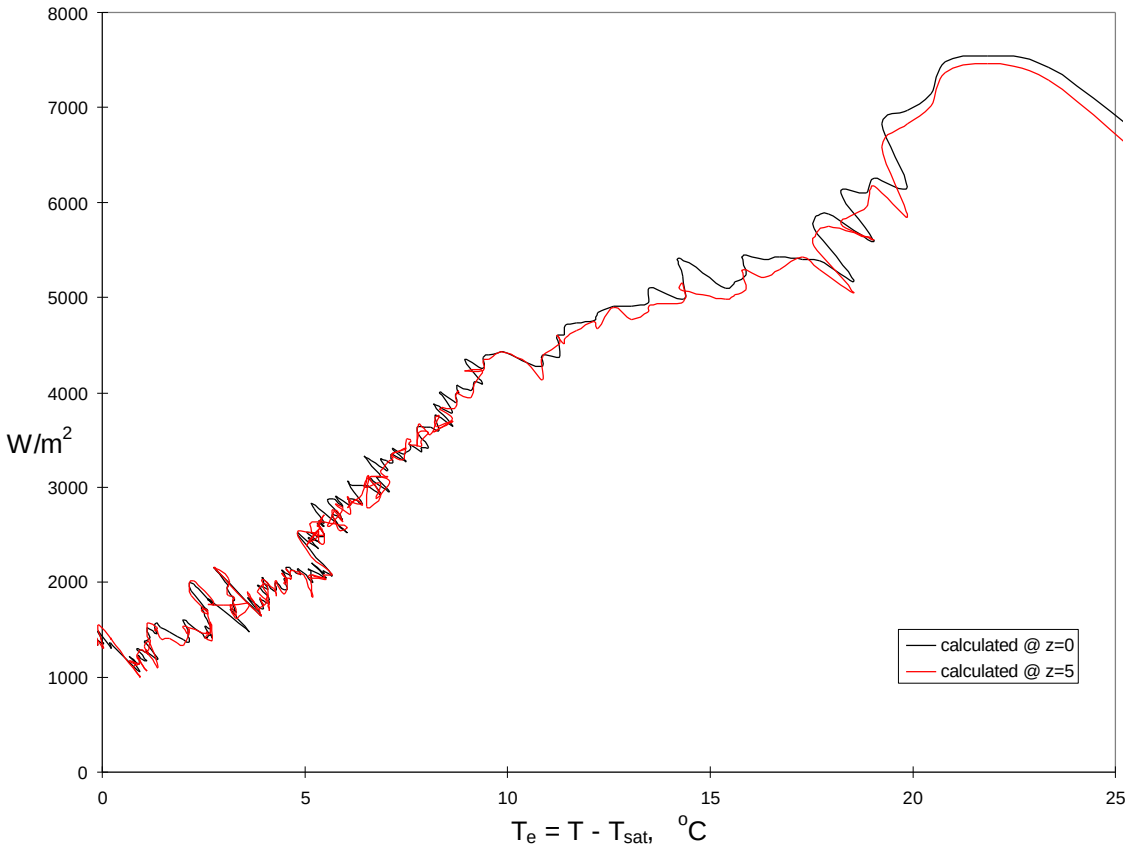


*Figure 5.4: Heat flux vs excess temperature at surface.*

Plotting the heat flux against surface temperature, as has been done in Figure 5.4, helps to identify the coupled influence of flow and boiling regimes. Since the surface temperature declined rapidly while data were recorded once per second, the temperatures closer to saturation temperature have more detail. Even so, the cyclic fluctuations of temperature near $20^{o}$ excess temperature has been interpreted as a zone of instability where churn flow caused vapor to push liquid upward and then gravity caused the liquid to fall back. This behavior has been observed in the video tape recording of this experiment. The video also showed that the flow was actually two-dimensional, with liquid and vapor moving laterally as well as vertically as they exchange momentum. Again, the heat flux measured from saturation temperature up to about $10^{o}$ excess temperature revealed a roughly linear relation, while the nature of the relation between excess temperature and heat flux is nonlinear at higher temperatures.

Generally, different types of flow were observed visually at different times and locations during the experiment. Also, the rate of boiling and the resultant stability of flow seems to have been reflected in the temperatures measured.

### 5.1.3 Boiling/Flow Regimes

The term "boiling regime" has been used to characterize the heat transfer mechanism at the boundary of an impermeable surface and a discrete channel, or fracture. The term "flow regime" has been used to describe the mechanics of the fluid motion in an interval of the fracture that is distinct from the fluid flow at other locations. Observation shows that flow regimes influence the heat flux to the boundary of the flow, and the heat flux affects the mechanics of the fluid motion by generating vapor at the margins of flow. Figure 5.5 helps to describe the relations between boiling and flow regimes.

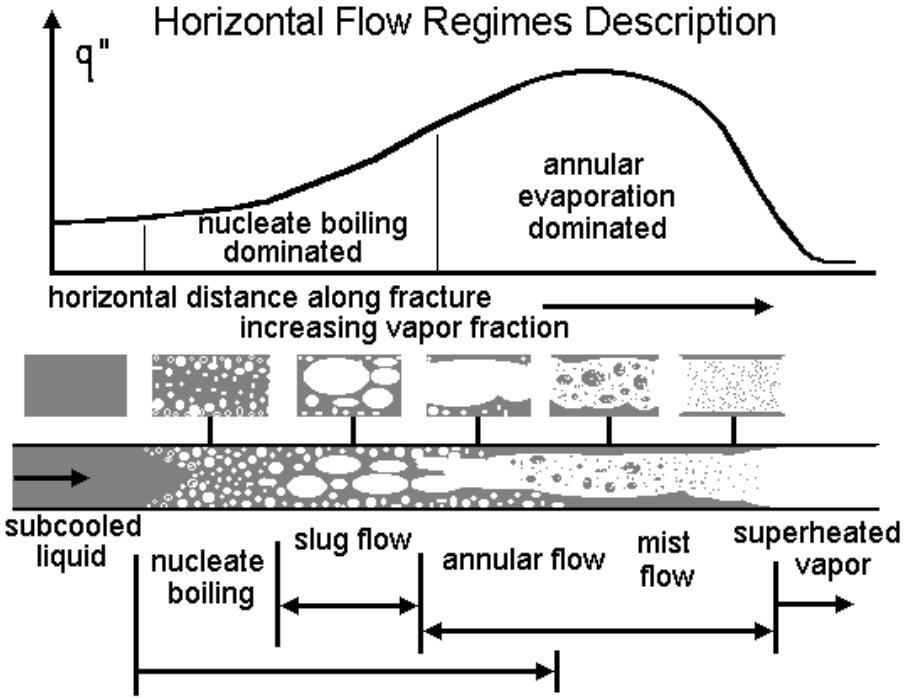


*Figure 5.5: A qualitative description of boiling and flow regimes.*

Limited analogies to flow in tubes and channels have been considered in the development of Figure 5.5. The effects of severe roughness, variable fracture aperture, and the porous nature of rock surfaces have been neglected in this simple illustration, however, the figure can be useful for a general description of injection into a horizontal fracture. Near the injection location the liquid is subcooled, and heat from the matrix begins a boiling process that proceeds from bubbly flow, to slug flow where bubbles coalesce, into annular and mist flow until the moving fluid becomes completely vaporized. The boiling regimes in this illustration are divided into nucleate boiling and film evaporation.

In Figure 5.5, nucleate boiling begins at the margins of the flow and generates bubbles that migrate into the main channel of flow. This occurs at relatively low quality, that is, at relatively small vapor fractions in the flow. As quality increases the mean velocity of the flow increases with the decreasing mean density of the fluid. The annular flow, therefore,

may occur with exchanges of momentum between the liquid and vapor fluxes and liquid droplets can become entrained in the vapor flow. As further evaporation occurs, annular film evaporation may become the boiling mechanism at relatively higher fractions of vapor in the channel. Annular film evaporation is a mass flux from the liquid to a vapor phase without the nucleation of bubbles across a thin film of liquid at the margin. In the horizontal orientation shown, the liquid and vapor can segregate due to density differences and the boundary conditions for heat transfer from above and below the fracture can be different.

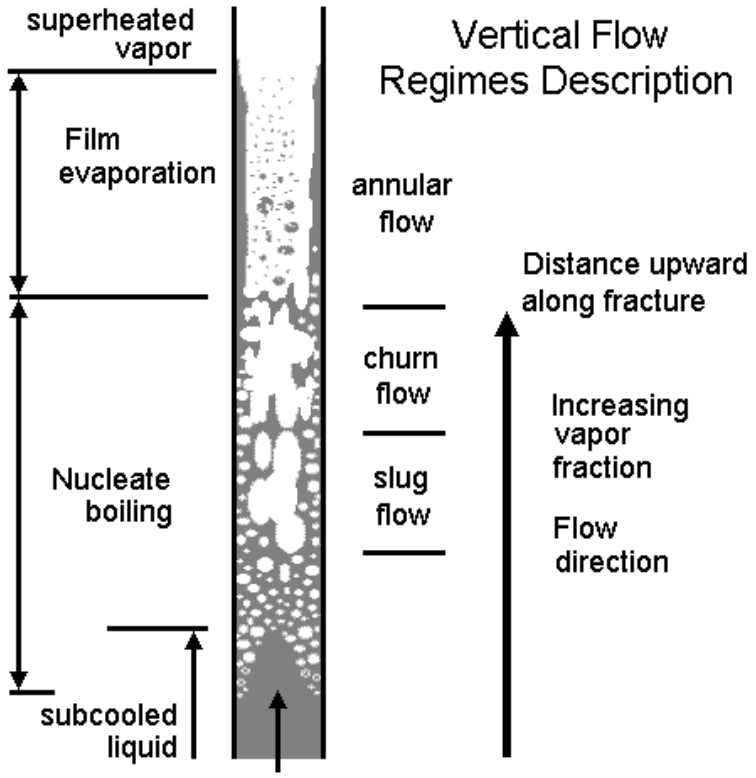


*Figure 5.6: Boiling and Flow regimes in a vertical fracture.*

Figure 5.6 is a similar illustration of upward vertical flow. In this illustration the effect of gravity does not cause a segregation of flow, but does exert differential force on the liquid and vapor phases. In vertical flow the buoyancy of the vapor and the interfacial tension allow the slugs of vapor to push slugs of liquid upward. Under the conditions where these forces were in relative equilibrium, instability in the flow was observed in the laboratory. This is illustrated as the churn flow regime in this figure.

To summarize, the morphology of a flow regime depends, in part, on how the boiling mechanism at the boundary adds vapor to the flow, and the boiling regime depends upon the vapor fraction of the fluid and how this interacts with the boundaries. Interest in the effect of fracture orientation on flow regime, and the uncertainty of how fracture aperture

dimension may restrict boiling and flow regimes led to the development of a new experimental apparatus this past quarter.

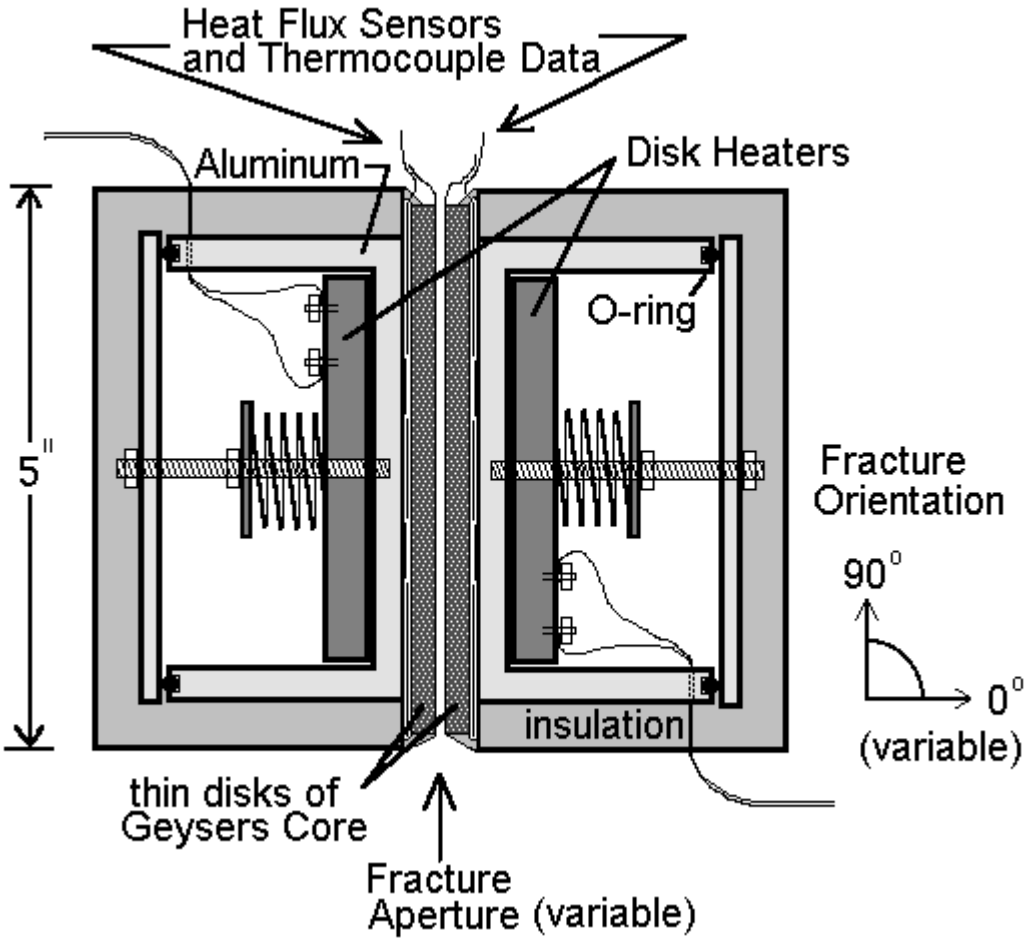


*Figure 5.7: A new experimental apparatus to investigate boiling in real rock surfaces.*

## 5.2 STEADY STATE BOILING EXPERIMENT

The assembly shown in Figure 5.7 was constructed this past quarter to investigate boiling on real rock surfaces with experimental control of the fracture aperture and orientation with free convective boiling. Controlled experiments will begin in the spring quarter, but some preliminary study has been performed to make sure the apparatus operates as planned when immersed in water. After one preliminary experiment, it has.

The apparatus will be operated by immersion into a tank of degassed water, and the temperatures on both sides of the thin disks of rock core will be monitored. Heat flux sensors will also be used to quantify the heat flux to the aperture between the rock slices. The power supplied to the heaters in the assembly will be increased incrementally in stages to allow boiling to occur within the fracture in a steady state fashion. Shims of precisely measured thickness will be used to control the aperture between the rocks, and the assembly includes a structure that allows it to rotate and hold any angle from horizontal to vertical.

### 5.2.1 Discussion

A continuation of experimentation has led to the investigation of inertia, viscous, buoyancy and interfacial forces that influence two phase flow and boiling in a fracture. A quantification of these influences has been necessary for reducing the coupling of flow and heat flux in a boiling fracture to something that might be possible to model. The general approach has been to seek an empirical description of a boiling convection coefficient to relate the heat flux to a fracture surface as a function of the excess temperature at the surface. Continuing work with the transient experiments, and new work with steady state boiling will help to determine the physical circumstances that significantly influence boiling and flow regimes.

# 6. MODELING OF GEOTHERMAL RESERVOIRS CONSTRAINED TO INJECTION RETURN DATA

This project is being conducted by Research Assistant Ma. Michelle Sullera and Prof. Roland Horne. The aim is to deduce injection return mechanism(s) and flow paths from correlations between producer chloride concentration and injection operating parameters (flow rate and injection chloride).

## 6.1 BACKGROUND

Previously, it was found that chloride data sets from both Palinpinon-I geothermal field in the Philippines and Dixie Valley field are best modeled by:

$$Cl_p = a_0 + a_1 Q_{I1} + a_2 Q_{I2} + a_3 Q_{I3} + \ldots + a_n Q_{In} + bt \qquad (6.1)$$

where $Cl_p$ = chloride concentration in production well, P

$Q_{In}$ = mass flow rate to injection well, In

$a_n$ = linear coefficient of well In

$a_0$ = a constant associated with local chloride concentration

$t$ = time

Comparison of the coefficients obtained showed that this model is dominated by the time term: for Dixie Valley, injection rate coefficients ($a_n$'s) are less than 0.005% of time coefficient ($b$) and, for Palinpinon injection rate coefficients are approximately 4% of time coefficient. To assess the contribution of changes in injection rates to changes in producer chloride concentration we need to isolate the underlying trend of chloride with time. This trend may or may not be linear as was assumed in the original model. Wavelet decomposition, discussed in the next section, addresses the issue of determining the time trend in general.

Also, model (6.1) gave correlation coefficients ( R ) very close to one but had poor predicting capacity. Upon closer examination it was found out that this was due to the insufficient amount of data used in the analysis. Tabachnick (1996) gave the following rules of thumb regarding the number of data points required: $N > 50 + 8m$ for testing the multiple correlation and $N > 104 + m$ for testing individual predictors ($N$ is the number of data points and $m$ is the number of predictors/parameters in the linear model.) It was typical in the previous analysis to have less than half the sufficient number of data points. Consequently, this resulted in regression solutions that fit the chloride data exceptionally well but predict succeeding values poorly. The fit was perfect - but meaningless. Fortunately, a larger data set from Palinpinon has been made available to us by PNOC-EDC and we will use this set for all succeeding analyses.

## 6.2 ANALYSIS USING WAVELETS

Wavelet decomposition is the separation of a function to its detail and approximation. After removing the kinks and wiggles (detail) from a function, one arrives at a smoother version of the function (approximation). Fig. 6.1 illustrates the concept using the chloride concentration function from well OK-7D. In essence, wavelet decomposition is similar to Fourier transform analysis; only, in Fourier transform analysis the details and approximation of a function are expressed as sines and cosines instead of the various wavelet functions used in wavelet decomposition. Mathematical procedures for wavelet decomposition are discussed by Ogden (1997).

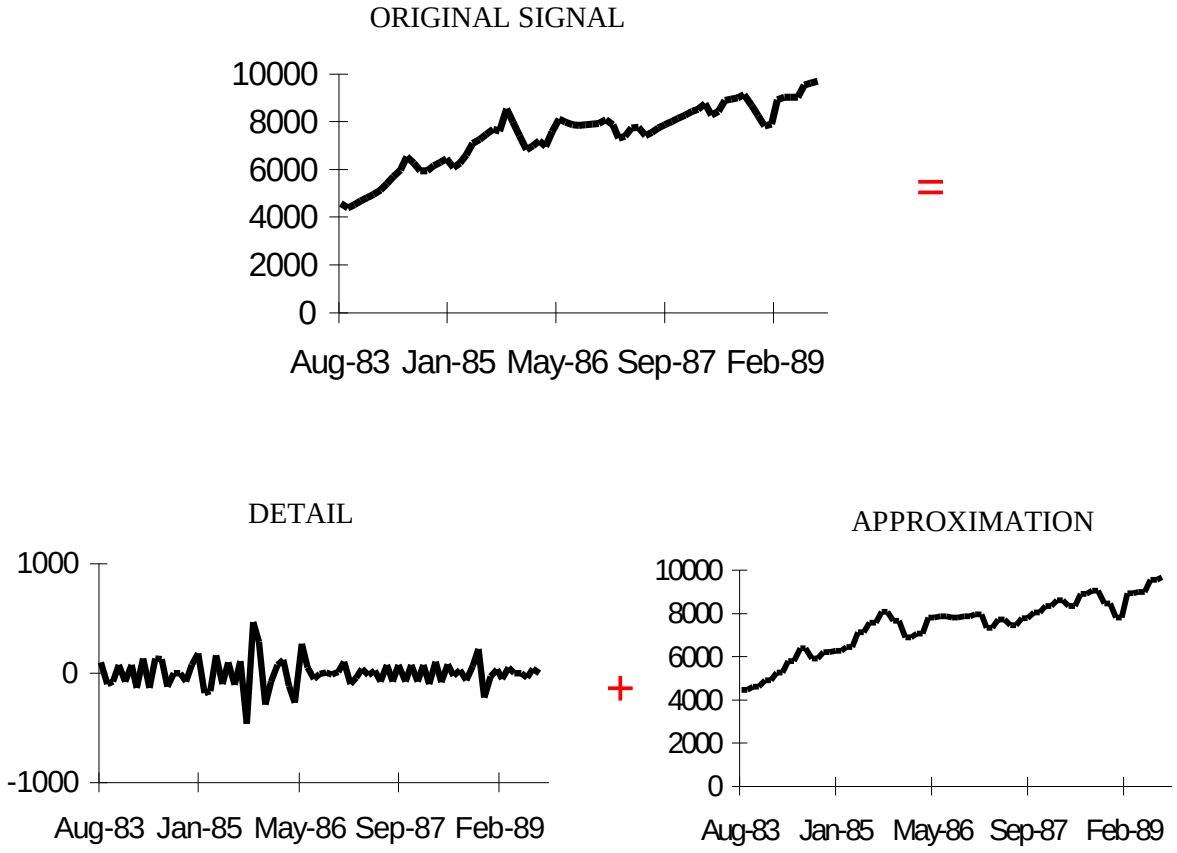


*Fig. 6.1 Level 1 wavelet decomposition of chloride signal from OK-7D (wavelet: Haar)*

During successive decompositions, high "frequency" details are removed first and the resulting approximation is again subjected to a decomposition. After removing the four highest frequency details (Fig. 6.2) from the chloride concentration function of well OK-7D, the general trend of chloride with time becomes readily evident in the resulting approximation function (Fig. 6.3). Fig. 6.3 shows that the general trend in chloride is nonlinear, contrary to the assumption used in the previous model (Eqn. 6.1)

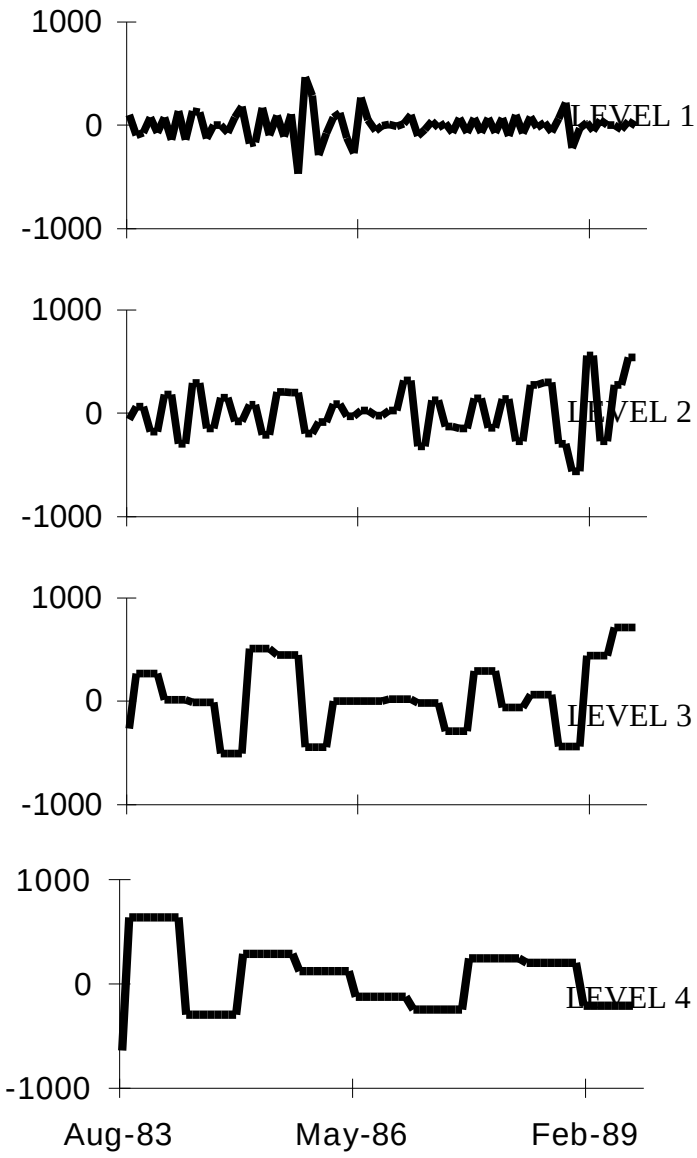


*Fig. 6.2 Detail functions for OK-7D chloride (levels 1, 2, 3, and 4).*

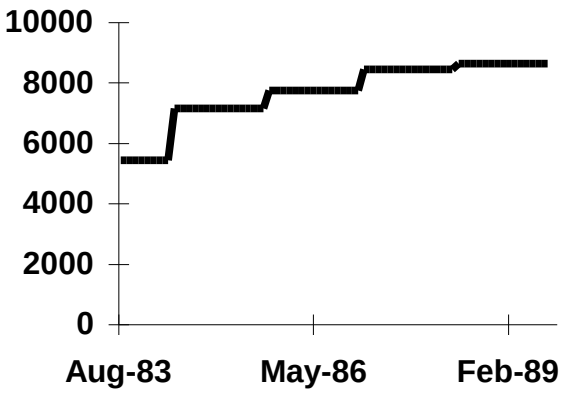


*Fig. 6.3 Level 4 approximation to OK-7 chloride.*

A useful way of looking at details is by interpreting them as deviations of the original signal from the approximation. In the current example, the original signal is given as monthly values of chloride. The approximation resulting from the first decomposition estimates constant chloride values over intervals of two months and the details give changes in monthly chloride. Indeed, it is these changes over and above the underlying trend that we want to monitor and correlate with the changes in injection rate. We have thus decomposed the injection rate functions into their respective details and approximations. Next, the multiple linear model previously used in analyzing the undecomposed signals will be adapted to the analysis of the details:

$$Cl_p = \quad a_1 Q_{I1} + a_2 Q_{I2} + a_3 Q_{I3} + \ldots \quad + a_n Q_{In} \qquad (6.2)$$

where $Cl_p$ = chloride concentration detail in production well, P

$Q_{In}$ = injection rate detail in well In

$a_n$ = linear coefficient of well In

The next issue to address would be the choice of detail level to investigate. It seemed reasonable at first to assume that the best choice is the one which will give the highest multiple regression coefficient (R). Investigation of the regression coefficients obtained from modeling the chloride details of OK-7D invalidated that assumption. Table 6.1 shows that at level 4 the regression coefficient becomes unity signifying a perfect correlation; and, correlation at succeeding levels remain perfect. As the decomposition level goes up, the detail will have longer time intervals with constant values. This effectively reduces the amount of data to be modeled and results to perfect, meaningless correlation. The choice is thus narrowed down to levels 1, 2, and 3.

*Table 6.1 Correlation coefficients for multiple linear regression on OK-7D chloride detail.*

| Detail Level | Multiple R |
|---|---|
| 1 | 0.581 |
| 2 | 0.579 |
| 3 | 0.927 |
| 4 | 1.000 |
| 5 | 1.000 |

Table 6.2 shows the statistics for level 1, 2, and 3 regression. The all-positive coefficients from level 1 and 2 regression (negative coefficients in level 2 may be eliminated using further statistical hypothesis testing) make interpretation easier.

*Table 6.2 Regression statistics for multiple linear regression on OK-7D chloride detail (levels 1, 2, and 3).*

| | LEVEL 1 | LEVEL 2 | LEVEL 3 |
|---|---|---|---|
| **Multiple R** | **0.581136875** | **0.579245435** | **0.927648988** |
| **R Square** | **0.337720068** | **0.335525274** | **0.860532646** |
| **Adjusted R Square** | **0.25376909** | **0.251296083** | **0.842853685** |
| **Standard Error** | **378.0858057** | **329.8556639** | **162.9793011** |
| **Observations** | **81** | **81** | **81** |
| | | **COEFFICIENTS** | |
| **Intercept** | **28.50768123** | **38.64745752** | **29.92678358** |
| **X Variable 1** | **4.292302316** | **1.385430725** | **0.014481522** |
| **X Variable 2** | **6.69666669** | **10.30242782** | **-7.031416109** |
| **X Variable 3** | **3.447978105** | **-0.657946093** | **-10.50567914** |
| **X Variable 4** | **1.695344748** | **-0.217551717** | **19.17474584** |
| **X Variable 5** | **16.6456427** | **4.680772865** | **22.89584503** |
| **X Variable 6** | **4.507393431** | **1.879373824** | **7.674570245** |
| **X Variable 7** | **1.90734605** | **6.644213655** | **0.029831362** |
| **X Variable 8** | **0.77110963** | **0.38640786** | **2.305292538** |
| **X Variable 9** | **0.154506734** | **-0.591562894** | **-9.226884793** |

On the other hand, the correspondence between changes in chloride and changes in injection rates are more readily visible at level 3. In Fig. 6.4 the level 3 details of injection wells PN-6RD and PN-9RD closely follows the detail of OK-7D chloride during intervals when injection to these wells are high.

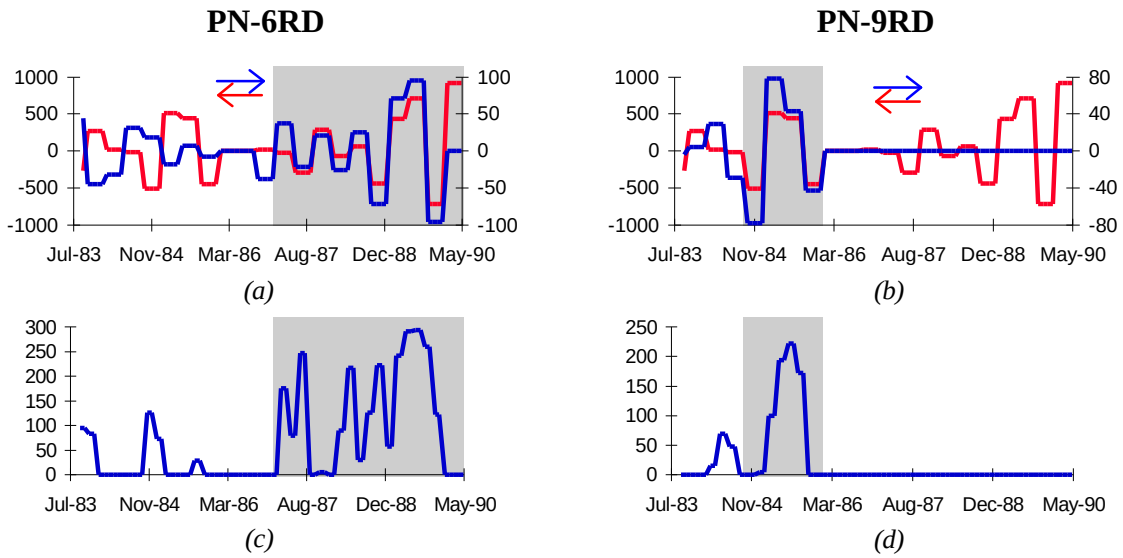


*Fig. 6.4 (a) Level 3 detail of OK-7D chloride - red; level 3 detail of PN-6RD injection rate - blue. (b) Level 3 detail of OK-7D chloride - red; level 3 detail of PN-9RD injection rate -blue. (c) PN-6RD injection rate. (d) PN-9RD injection rate.*

## 6.3 NEXT STEP

Having no compelling reason to choose one detail level over another, regression analysis will be completed for detail levels 1, 2, and 3. In conjunction with the resulting well coefficients ($a_n$s in Eq. 6.2) simple (univariate) regression coefficients for each well will also be compared to deduce injection flow paths and well connections.

## 7. REFERENCES


Ambusso, W.J., Satik, C., and Horne, R.N., 1996. A Study of Relative Permeability for Steam-Water Flow in Porous Media. Proc. of 21st Stanford Workshop on Geothermal Reservoir Engineering.

Ambusso, W.J., 1996. Experimental Determination of Steam-Water Relative Permeability Relations. MS Thesis, Stanford University, Stanford. Calif.

Cohen, L. D. and Cohen, I. : "A Finite Element Method Applied to New Active Contour Models and 3D Reconstruction from Cross Sections." *Proceedings 3rd International Conference on Computer Vision, Osaka, Japan*.

Finsterle, S., Pruess, K., Bullivant, D.P., and O'Sullivan, M.J., 1997. Application of Inverse Modeling to Geothermal Reservoir Simulation, Proc. of 22nd Workshop on Geothermal Reservoir Engineering, Stanford, Calif.

Johns, R. A.: "Diffusion and Dispersion of Solute in a Variable Aperture Fracture", 1991, Ph. D. dissertation, Stanford University

Kass, M., Witkin, A. and Terzopoulos, D.: "Snake: Active Contour Models", *International Journal of Computer Vision*, 1987

Ogden, R.T., 1997, Essential Wavelets for Statistical Applications and Data Analysis. Birkhauser Boston, Cambridge, MA.

Pratt, W. K.: "Digital Image Processing", 1991, JohnWiley & Sons, Inc.

Pruess, K., 1991. TOUGH2-A General Purpose Numerical Simulator for Multiphase Fluid and Heat Flow, Report LBL-29400, Lawrence Berkeley National Laboratory, Berkeley, Calif.

Satik, C., 1998. A Study of Steam-Water Relative Permeability. SPE 46209, paper prepared for presentation at the 1998 SPE Western Regional Meeting, Bakersfield, CA, 10–13 May.

Satik, C., 1997, A Study of Boiling in Porous Media, Proc. 19th New Zealand Geothermal Workshop, Auckland, NZ.

Satik, C., 1998, A Measurement of Steam-Water Relative Permeability, Proc. of 23rd Workshop on Geothermal Reservoir Engineering, Stanford, Calif.

Satik, C., Ambusso, W.J., Castanier L.M. and Horne, R.N., 1995. A Preliminary Study of Relative Permeability in Geothermal Rocks, GRC Trans. Vol. 19, pp 539.

Tabachnick, B.G. and Fidell, L.S., 1996, *Using Multivariate Statistics*. Harper Collins College Publishers, New York.